Environmental Controls of InSAR-Based Periglacial Ground Dynamics in a Sub-Arctic Landscape

Rouyet, L.

2021-07

Author Contributions:
Conceptualization: L. Rouyet, O. Karjalainen, J. Hjort
Data curation: L. Rouyet, O. Karjalainen, P. Niittynen
Formal analysis: L. Rouyet, O. Karjalainen
Funding acquisition: L. Rouyet, J. Aalto, M. Luoto, T. R. Lauknes, J. Hjort
Investigation: L. Rouyet, O. Karjalainen

Environmental Controls of InSAR-Based Periglacial Ground Dynamics in a Sub-Arctic Landscape

L. Rouyet[1,2,3] , O. Karjalainen[4] , P. Niittynen[5] , J. Aalto[5,6] , M. Luoto[5] , T. R. Lauknes[1,2] , Y. Larsen[1] , and J. Hjort[4]

[1]NORCE Norwegian Research Centre AS, Tromsø, Norway, [2]Department of Geosciences, The Arctic University of Norway (UiT), Tromsø, Norway, [3]Arctic Geology Department, The University Centre in Svalbard (UNIS), Longyearbyen, Norway, [4]Geography Research Unit, University of Oulu, Oulu, Finland, [5]Department of Geosciences and Geography, University of Helsinki, Helsinki, Finland, [6]Weather and Climate Change Impact Research, Finnish Meteorological Institute, Helsinki, Finland

Abstract Periglacial environments are characterized by highly dynamic landscapes. Freezing and thawing lead to ground movement, associated with cryoturbation and solifluction. These processes are sensitive to climate change and variably distributed depending on multiple environmental factors. In this study, we used multi-geometry Sentinel-1 Synthetic Aperture Radar Interferometry (InSAR) to investigate the spatial distribution of the mean annual ground velocity in a mountainous landscape in Northern Norway. Statistical modeling was employed to examine how periglacial ground velocity is related to environmental variables characterizing the diverse climatic, geomorphic, hydrological and biological conditions within a 148 km² study area. Two-dimensional (2D) InSAR results document mean annual ground velocity up to 15 mm/yr. Vertical and horizontal velocity components in the East–West plane show variable spatial distribution, which can be explained by the characteristics of cryoturbation and solifluction operating differently over flat and sloping terrain. Statistical modeling shows that slope angle and mean annual air temperature variables are the most important environmental factors explaining the distribution of the horizontal and vertical components, respectively. Vegetation and snow cover also have a local influence, interpreted as indicators of the ground material and moisture conditions. The results show contrasted model performance depending on the velocity component used as a response variable. In general, our study highlights the potential of integrating radar remote sensing and statistical modeling to investigate mountainous regions and better understand the relations between environmental factors, periglacial processes and ground dynamics.

Plain Language Summary In cold regions, freeze and thaw cycles lead to movement in the upper part of the ground. The landscape distribution of these movements depends on several environmental conditions, such as the local climate, topography, vegetation, material type and soil moisture. Here we mapped millimeter to centimetre mean annual ground velocities using a measurement technique based on satellite radar images. We analyzed how the environmental conditions are related to the distribution of the ground velocity at the landscape scale. Statistical models were applied to relate the ground velocity to environmental conditions at similar locations and showed that the spatial variability of the air temperature and the slope inclination are the two main controlling factors. Vegetation and snow cover have also an indirect effect due to their link with the ground material and moisture conditions. In general, the study contributes to the development of approaches integrating remote sensing and modeling techniques to cover large and hard-to-access mountainous regions and provide new insights on the processes shaping the landscape in cold environments.

1. Introduction

Cold polar and mountainous regions encompass a broad range of frost-driven processes that shape the landscape. Characterized by seasonally or perennially frozen ground (permafrost), these so-called periglacial environments are highly dynamic (French, 2007) and especially sensitive to climate change (Aalto et al., 2017; Biskaborn et al., 2019; Hjort et al., 2018). Seasonal ground freezing and thawing in the upper part of the ground cause heave and subsidence due to water-to-ice phase change (Bonnaventure & Lamoureux, 2013; Thomas et al., 2009). On periglacial slopes, mass wasting processes driven by gravity induce downslope

Methodology: L. Rouyet, O. Karjalainen, T. R. Lauknes, Y. Larsen
Project Administration: L. Rouyet, O. Karjalainen, T. R. Lauknes, J. Hjort
Software: L. Rouyet, O. Karjalainen, T. R. Lauknes, Y. Larsen
Supervision: J. Aalto, M. Luoto, T. R. Lauknes, J. Hjort
Visualization: L. Rouyet, O. Karjalainen
Writing – original draft: L. Rouyet, O. Karjalainen
Writing – review & editing: P. Niittynen, J. Aalto, M. Luoto, T. R. Lauknes, Y. Larsen, J. Hjort

movement (Harris, Kern-Luetschg, et al., 2008; Matsuoka, 2001). When considering slow deformation of unconsolidated material over flat areas and slopes, periglacial processes are respectively referred to as cryoturbation and solifluction (French, 2007). On flat areas covered by thin fine-grained unconsolidated deposits and low ice content, the ground typically heaves and subsidies with a millimetric to centimetric seasonal amplitude (Gruber, 2020; Matsuoka et al., 2003; Smith, 1987). On slopes, millimetric to centimetric solifluction annual rates (net downslope velocities) have been measured in subarctic areas and mid-latitude mountainous regions with seasonal frost or warm permafrost conditions (Ballantyne, 2013; Harris, Kern-Luetschg, et al., 2008; Matsuoka et al., 1997; Ridefelt et al., 2009). At local to regional scales, a large set of climatic (temperature, precipitation), geomorphic (topography, substrate type), biological (vegetation type), and hydrological factors (soil moisture/water content) have an influence on the spatio-temporal dynamics of the ground (Etzelmüller et al., 2001; Guglielmin et al., 2008; Harris et al., 2003; Hinzman et al., 1991). Changing environmental conditions modify the periglacial ground dynamics, which can impact infrastructure and ecosystems (Harris et al., 2009; Hjort et al., 2018; Jorgenson et al., 2001; Nelson et al., 2002). However, the complexity of the relations between the environmental conditions (controlling factors), the periglacial processes (causes), the ground dynamics and the induced landforms (effects), makes the future impacts challenging to assess (Knight & Harrison, 2013).

Traditionally, geomorphological studies and monitoring of periglacial processes are conducted by in-situ field mapping and measurements (Harris et al., 2009; Romanovsky et al., 2010; Shiklomanov et al., 2012). These observations are often difficult to perform and usually provide sparse and unevenly distributed measurement data. Over the last decades, satellite remote sensing has become a valuable tool to map and monitor periglacial landforms, especially in remote and hard-to-access mountainous areas and Arctic regions (Kääb et al., 2005; Westermann et al., 2015). Repeat-pass satellite Synthetic Aperture Radar Interferometry (InSAR) enables the quantification of ground displacements over large areas. InSAR allows for measuring submillimetre to centimetre sensor-to-ground distance changes derived from the phase differences detected between Synthetic Aperture Radar (SAR) images acquired at different times (Massonnet & Feigl, 1998). InSAR measurements are along the radar line-of-sight (LOS) and thus intrinsically one-dimensional. The Sentinel-1 SAR mission of the European Commission Copernicus Program follows a sunsynchronous polar orbit, and observes at an oblique incidence angle toward East (ascending passes) or West (descending passes). Thus, the radar is nearly blind to horizontal North–South displacements, but by combining InSAR results from the two satellite geometries, 2D information in the vertical E–W plane can be estimated (Eriksen, Lauknes, et al., 2017). InSAR has been intensively used to map moving landforms in mountainous regions (Barboux et al., 2014, 2015; Dini et al., 2019). Several studies have also analyzed InSAR-detected periglacial ground displacements against environmental variables. They demonstrated that the spatio-temporal variability of InSAR results can be related to the air and ground temperature (Bartsch et al., 2019; Strozzi et al., 2018), the thickness of the active layer (Liu et al., 2012; Wang et al., 2018), the water/ice content (J. Chen, Wu, et al., 2020; Daout et al., 2017), and the surficial geology (Rouyet et al., 2019; Rudy et al., 2018). The findings show that InSAR has not only a value to identify moving landforms, but also the potential to indirectly document the spatio-temporal patterns of environmental variables controlling periglacial processes (Rouyet et al., 2019). However, the strong spatial heterogeneities characterizing mountainous areas lead to a large variability and combination of processes over short distances (Haeberli et al., 2010). Relating detected moving areas to actual geomorphological processes and their drivers can therefore be a challenging task.

To exploit remotely sensed information for the interpretation of environmental controls of ground dynamics, modern empirical techniques are required to analyze large datasets at regional to global scales. This has been made possible by the development of advanced statistical methods. Several studies have shown the potential of statistical modeling to estimate permafrost distribution (Aalto, Karjalainen, et al., 2018; Boeckli et al., 2012; Etzelmüller et al., 2001; Gruber & Hoelzle, 2001) and to capture the multivariate nature of periglacial processes at landscape-scale by documenting how their distribution and dynamics are influenced by environmental factors (Hjort & Luoto, 2011, 2013; Hjort et al., 2014; Karjalainen et al., 2019; Rudy et al., 2017). By statistically identifying the variables influencing the ground thermal regime and periglacial processes, it becomes possible to better explain their current distribution and predict their future evolution based on climate change scenarios (Aalto et al., 2017; Blois et al., 2013; Hjort et al., 2018; Karjalainen et al., 2020). However, previous research has been primarily based on in-situ measurements (e.g.,

ground temperature from boreholes) or mapped landforms (e.g., inventory of solifluction lobes and palsas) and few studies have integrated advanced remote sensing data documenting periglacial activity, such as InSAR-based ground velocity.

Here we examine the environmental controls associated with the spatial variability of mean annual ground velocities derived from Sentinel-1 InSAR measurements in a sub-arctic landscape. We use statistical multivariate modeling to relate the response variables (horizontal, vertical and combined 2D velocities) to seven environmental factors represented with geospatial data. To our knowledge, this is the first study to analyze InSAR results using spatially explicit statistical modeling. Specifically, we aim to a) document the distribution of ground velocity associated with cryoturbation and solifluction in a mountainous environment in Northern Norway, b) examine the relative importance and effects of the environmental factors on the periglacial ground dynamics, and c) discuss the limitations and implications of our findings in the context of periglacial research.

2. Study Area

The study area is located in the Gaissane mountain massif in the county of Troms and Finnmark, Northern Norway (70°00′N, 26°14′E). The region is part of the subarctic zone, characterized by long cold winters and short cool summers (NCCS, 2021). Northern Norway is affected by a large climatic gradient between the temperate and humid coasts and the cold and dry continental interior. The permafrost follows a similar distribution. The limit of the discontinuous zone, where permafrost is underlying 50%–90% of the landscape, is around 1,000 m a.s.l in the North-West and decreases below 400 m a.s.l. toward South-East (Farbrot et al., 2013; Gisnås et al., 2017). Both direct observations and physical models indicate that permafrost in Northern Norway is mainly warm (temperature above −3°C), and variably distributed depending on the vegetation and snow cover (Farbrot et al., 2008; Isaksen et al., 2008). In-situ measurements indicate that the permafrost has warmed and degraded (Christiansen et al., 2010; Isaksen et al., 2007), and models project that this trend is likely to continue for the next decades (Gisnås et al., 2013; Farbrot et al., 2013).

The study area consists of ca. 148 km^2 (Figure 1). The topography is characterized by two mountain massifs (Rásttigáisá at 1,066 m a.s.l and Geaidnogáisá at 1,038 m a.s.l) separated by a 2-km wide and 0.5-km deep NW-SE valley. The area has a large altitudinal gradient between 122 m a.s.l and 1,066 m a.s.l. The bedrock is composed of Precambrian crystalline rocks and layers of shales (Hyolithus zone), covered by peat, fluvial sediments, glacial till and boulder fields (Niittynen & Luoto, 2018). The study area has a mean annual air temperature below zero (−0.3 to −5.7°C; 1981–2010) and a mean annual precipitation sum between 457 and 669 mm (Aalto et al., 2017). The altitudinal gradient leads to a large spatial variability of the mean annual air temperature within the area (Aalto et al., 2017). Due to the complex local topography, the snow accumulates unevenly, and the snow persistence pattern is highly variable (Niittynen, Heikkinen, et al., 2018). Rásttigáisá-Geaidnogáisá area is part of the circumpolar arctic vegetation zone (Olson et al., 2001; Virtanen et al., 2016), at the transition between different main biomes of the northern high-latitude environment. The mountain birch forest line is at 250–350 m a.s.l., and thus, trees are only present in the lowest valleys.

According to the circum-arctic map of permafrost and ground-ice conditions (Brown et al., 2002), the study area is at the interface between the sporadic permafrost zone with medium ground ice content (10%–20%) and thick overburden (lowlands, highlands, and intra- and intermontane depressions), and the discontinuous permafrost zone with low ground ice content (0%–10%), thin overburden and exposed bedrock (mountains, highlands ridges, and plateaus). Kilometric products based on thermal remote sensing and physical modeling also show a large variability of the ground temperature, permafrost probability and active layer thickness (typically between 1 and 3 m) (Gisnås et al., 2017; Obu et al., 2019, 2020). Freeze and thaw processes lead to the development of a large range of periglacial landforms, such as patterned ground, peat plateaus, earth hummocks, and solifluction lobes (Martin et al., 2019; Seppälä, 2011).
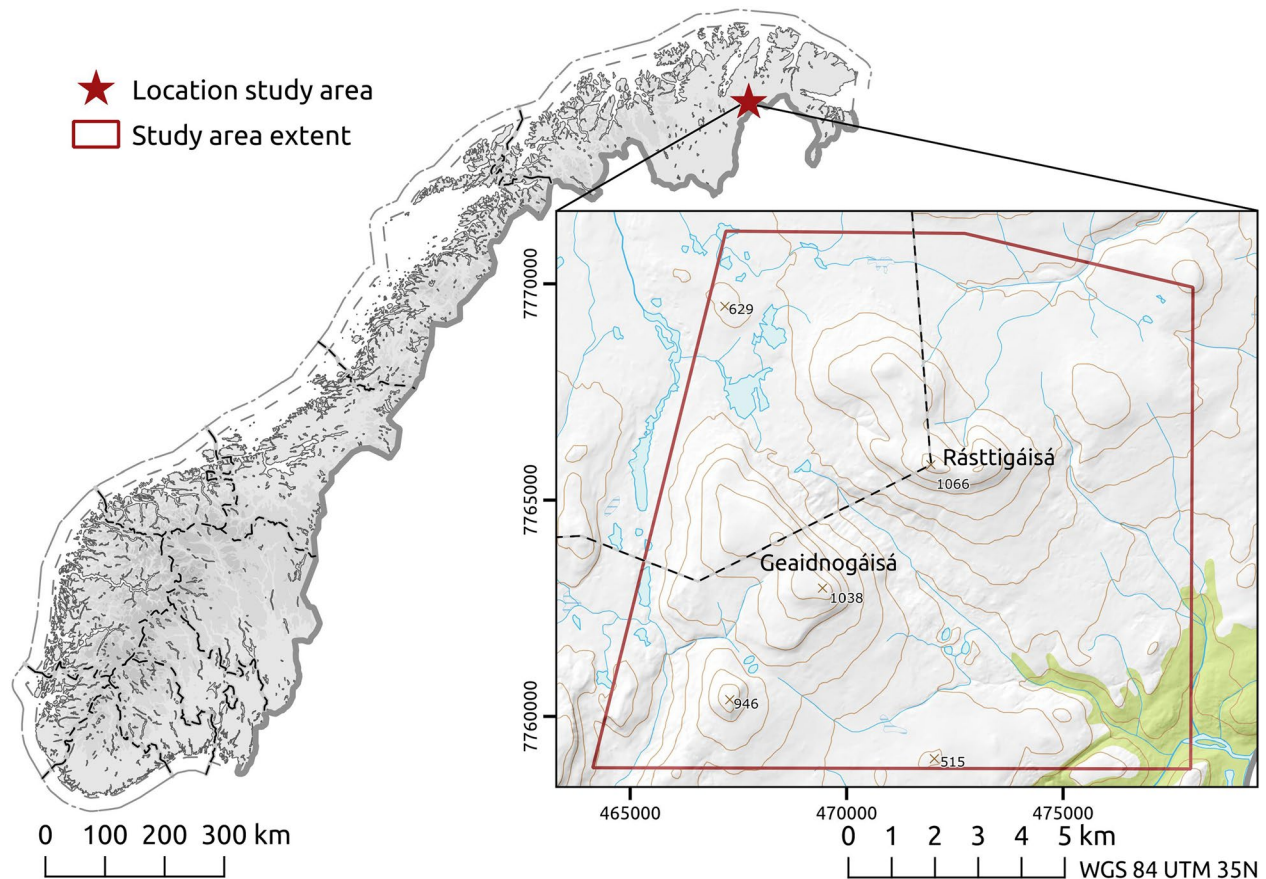
Figure 1. Location of the study area in Troms and Finnmark county (Northern Norway) centered around two mountains: Geaidnogáisá and Rásttigáisá. Background: topographical map of the Norwegian territory (NMA, 2020a). Brown lines: 100 m elevation contour lines. Gray-black lines: administrative borders (dashed lines in inset: border between Tana and Lebesby municipalities).

3. Data and Methods

The study presents an analysis of InSAR-based 2D mean annual ground velocity maps using multivariate statistical modeling. 2D InSAR results (response variables, Section 3.1) document the ground dynamics associated with periglacial processes identified in the study area (field observations, Section 3.2). The response variables are related to seven explanatory variables describing the environmental conditions (Sections 3.3) using statistical models (Section 3.4). This provides new insights about the factors controlling the horizontal, vertical and combined 2D ground velocities associated with cryoturbation and solifluction (Figure 2).

3.1. InSAR Products as Response Variables

InSAR results are based on SAR images from the Sentinel-1 mission of the European Commission Copernicus Program. The selected Interferometric Wide swath Mode scenes were acquired between 2015 and 2018 (Table 1). A total of 72 scenes were used in ascending geometry (track 14), and 67 in descending geometry (track 124). The sensor looks obliquely downward (~30° between the normal to the Earth's surface and the beam; see LOS incidence angles in Table 1), toward ENE for ascending acquisitions and toward WNW for descending acquisitions (~74°N and ~286°N of compass directions, see LOS orientations in Table 1). The observation period lasts 1,236 days (06.03.2015–10.21.2018) but the dataset includes gaps in winter, as only scenes with little snow cover have been selected (June–October).

We applied an InSAR technique employing spatial averaging (multi-looking) to reduce noise from scattering mechanisms in nonurban areas (Berardino et al., 2002). InSAR results were processed using the NORCE GSAR software (Larsen et al., 2005). Single Look Complex (SLC) images were co-registered and
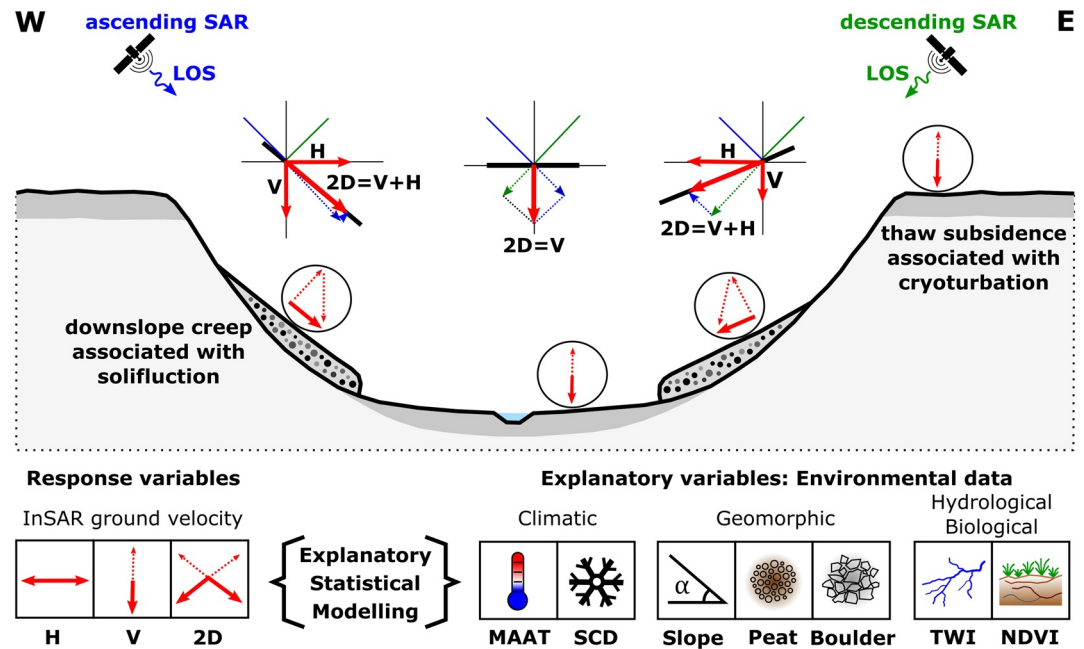
Figure 2. Conceptual scheme of the contribution of explanatory statistical modeling to relate ground dynamics documented by multi-geometry InSAR to environmental factors and provide new insights on the controls and effects of periglacial processes in mountainous landscapes. Dotted arrows show the expected components of the ground velocity associated with cryoturbation and solifluction. Solid bold arrows show the components that are measured using multi-annual 2D InSAR. The acronyms refer to Synthetic Aperture Radar (SAR), line-of-sight (LOS), vertical (V), horizontal (H), two-dimensional (2D), mean annual air temperature (MAAT), snow cover duration (SCD), topographic wetness index (TWI), and normalized difference vegetation index (NDVI).

multi-looked using a range/azimuth factor of 8×2, providing a ground resolution of ca. 40 m. We chose this multi-looking factor as a trade-off for preserving the highest resolution as possible, while avoiding reducing the reliability of the coherence estimate that decreases with low factors (Bamler & Hartl, 1998). Interferometric image pairs (interferograms) were generated with a maximal temporal baseline of 360 days, accounting for expected low velocities in the study area (mm–cm/year). The pairwise distance between the satellite positions at the acquisition times used for generating each interferogram, the so-called spatial baseline, has not been restricted. The effective maximal values (210 m for the ascending stack, 136 m for the descending stack) are clearly under the limit, for which there is no remaining spatial coherence (critical baseline, approximately 5 km for Sentinel-1). The small spatial baselines lead to small topographical component, which was estimated and removed using a 10 m DEM (NMA, 2016). The noise-level was reduced in all interferograms by applying a spatially adaptive coherence-dependent Goldstein filter (Baran et al., 2003; Goldstein & Werner, 1998). The datasets consist of 592 selected interferograms (SAR pairs) in ascending geometry and 471 in descending geometry (baseline plots in Supplemental Figures S1 and S2). Strongly decorrelated

Table 1
Properties of the Sentinel-1 SAR Images Used for InSAR Processing

SAR sensor	Frequency band (wavelength)	Time intervals for interferogram generation	SAR mode, track number and geometry	Number of selected scenes	Observation period (first-last selected scenes)	LOS orientation and incidence angle
Sentinel-1	C (5.55 cm)	6–360 days	IW, 14, ascending	72	06.03.2015–10.21.2018 (June–October)	74.2°
						30.4°
			IW, 124, descending	67	06.11.2015–10.05.2018 (June–October)	286.3°
						30.4°

Abbreviations: IW, interferometric wide swath mode; LOS, line-of-sight.

interferograms (mean coherence under 0.45) were removed, and pixels affected by layover were masked out. Pixels affected by low signal stability due to snow (e.g., perennial patches), water (e.g., lakes, rivers) or dense vegetation (e.g., forested areas) in most of the pairs were removed by applying a coherence-based filter (above 0.45 in at least 50% of the interferograms) (Berardino et al., 2002). If snow cover dominated in one acquisition, the coherence dropped and the interferograms based on that image were discarded. Similarly, if snow at one specific location was affecting too many interferograms in the stack (perennial patches), the pixel was discarded. Despite the relatively conservative thresholds, the effect of scattering mechanisms in coherent areas must be considered, as the differential propagation of the electromagnetic wave due to changing dielectric properties of the ground surface may lead to biased phase estimates. In high-latitude environments, one main limitation for InSAR is the snow (Zwieback et al., 2016). If the coherence dropped for isolated pixels in a limited amount of image pairs (e.g., early or late summer), wrong estimates may have been included in the results. As for snow, phase bias can occur due to volume scattering from ground moisture and biomass (De Zan et al., 2014; Zwieback & Hajnsek, 2014; Zwieback et al., 2015). However, the large stack and long temporal baseline used in the current study is expected to mitigate these effects (Ansari et al., 2020).

The conversion from cyclic to continuous phase differences, so-called unwrapping, is performed using the SNAPHU algorithm (C. Chen & Zebker, 2002). Due to the low velocity and good coherence in the study area, no major unwrapping errors have been identified in the processed interferograms. InSAR is a spatially relative technique, meaning that it must be calibrated to a reference location. The calibration is ideally performed using a point with a known velocity (Eriksen, Bergh, et al., 2017). In a remote environment where in-situ measurements are not available or not comparable to the resolution of the InSAR measurements, this is unfortunately often not feasible (Antonova et al., 2018). Different reference points were tested and a common reference for both datasets was chosen in an area assumed to be stable. It is located in the valley between Rásttigáisá and Geaidnogáisá (70°00"15.1""N 26°11"57.1"E, mapped in Figures 5 and 6), in flat terrain (<2° slope angle) with visible rock crop and little soil cover, leading to high InSAR coherence (>0.7 for both geometries). All InSAR results are spatially relative to this location. We estimated ground displacements using the Small Baseline Subset (SBAS) method (Berardino et al., 2002). The focus is placed on spatial distribution, and all results are based on averaged values. The phase inversion was performed using a linear deformation model. We solved for the mean annual ground velocity based on a L1-norm-based cost function, which is more robust than L2-norm with respect to unwrapping errors (Lauknes et al., 2011). For the atmospheric filtering, we used a spatial filter of 2,000 m spatial filter and a temporal filter of 120 days. The contribution from the stratified atmosphere was mitigated by a data-driven approach where we study the relation between residual phase and topography (Cavalié et al., 2007) using a Digital Elevation Model (DEM) at 10 m resolution (NMA, 2016). Based on a redundant set of interferograms, we further solved for the stratified delay per scene using a network-based approach (Lauknes, 2011). The initial InSAR ground velocity maps from both ascending and descending geometries were compared with results from the freely available InSAR Norway ground motion mapping service (Dehls et al., 2019; NGU, 2020). The processing is also based on Sentinel-1 images, but applies a Persistent Scatterer Interferometry (PSI) algorithm (Ferretti et al., 2001) that allows for preserving the full resolution of the images (5 × 20 m in range × azimuth). PSI results are based on different reference points and document another scattering mechanism than SBAS. They were used to qualitatively assess the general consistency of our results.

InSAR measurements from ascending and descending geometries correspond to one-dimensional (1D) sensor-to-ground distance change along the LOS. By combining both geometries, it is possible to estimate the 2D velocity in the vertical plane spanned by the ascending and descending LOS orientations, which approximately is E–W (Eriksen, Lauknes, et al., 2017). The results were also decomposed into vertical (Up–Down, U–D) and horizontal (East–West, E–W) components (Figure 2). It should be noted that the radar is still blind to displacements orthogonal to the LOS plane, which leads to an underestimation of the measurements in case of a large North–South (N–S) horizontal component. To avoid misinterpretation when analyzing gravity-driven processes such as solifluction, we masked out pixels in areas where a significant horizontal component toward N or S is expected (Rouyet et al., 2019). As reported by Matsuoka (2001), the slope angles of documented solifluction landforms can range from 2° to 41°. Based on this information, we masked out areas with slope angles over 2° and slope orientations ± 22.5° around 360° (N) and 180° (S) (compass directions 337.5°N–22.5°N and 157.5°N–202.5°N) (gray areas in Figure 3). All areas with slope angles below
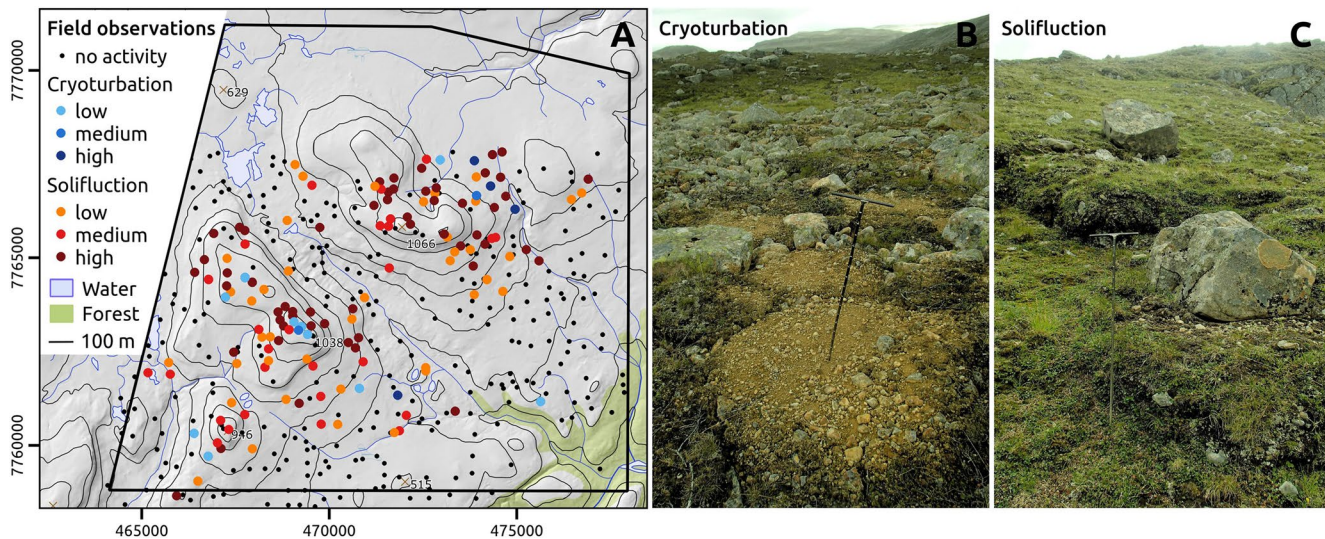
Figure 3. Field observation of cryoturbation and solifluction activity. (a) The field observation sites (dots) and locations where cryoturbation (blue dots) and solifluction (red dots) activity has been qualitatively rated as negligeable, low, medium, or high. Topographical data from NMA (2020a). (b) An example of field site with high cryoturbation activity. (c) An example of field site with high solifluction activity.

2° were included, assuming that they are mainly affected by a vertical component. All E–W slopes were included, assuming that they do not include a significant N–S component.

InSAR processing led to the development of three products, further used as response variables: 1) the horizontal velocity, 2) the vertical velocity, 3) the 2D velocity consisting in the combination of the two previous components. Considering the long total observation period (three years) and the relatively small extent of the study area (approx. 12 × 12 km), we estimate that the accuracy is well below 1 mm/yr (Supplemental Figure S3), assuming that atmosphere is the dominant noise source (Emardson et al., 2003). The closer to the reference point, the higher the accuracy. The results document mean velocities in mm/yr that are mostly designed for gradual multi-annual processes, such as the net downslope component of the solifluction. However, as no winter scenes are included, the InSAR results are mostly representative of the thawing periods, which emphasize the downward component of the cryoturbation. Prior to statistical modeling, all results were converted to absolute values to focus on the magnitude of the vertical, horizontal and combined 2D velocities, instead of their direction. The number of pixels where ground displacement is documented is 69,035, corresponding to ca. 74% of the study area (110 km^2). They were geocoded using a DEM at 10 m resolution (NMA, 2016). The final products have a 40 m ground resolution, documenting the averaged contribution of scatterers within the pixels. Although very fine-scale processes may not be captured by these medium resolution products, the results are assumed to be appropriate to assess the relative spatial variability of the ground dynamics in the study area and discuss their relations with environmental variables.

3.2. Field Observations of Cryoturbation and Solifluction

The cover of cryoturbation and solifluction (m^2) activity within 100 m^2 grids was mapped at 674 randomly selected field sites across the study area during the 2015–2016 summer seasons. The activity was visually estimated using indicators, such as vegetation density, lichen cover and frost disturbance, following the methodology presented in Hjort and Luoto (2009). Based on the field observations, the activity was then classified as negligible (<20 m^2), low (20–40 m^2), medium (40–60 m^2), and high (>60 m^2) for both processes. Solifluction is the dominant process in the area (Figure 3a). At 429 locations, the InSAR results overlap with field sites (at maximum one per pixel, Figure 3a) and the activity rating has been compared with the response variables to assess the relevance of the spatial variability of InSAR-detected ground velocity. A quantitative comparison is not feasible due to the differences of measure and spatial resolution between the remotely sensed (ground velocity within 40 × 40 m pixels) and field information (qualitative documentation of activity within 10 × 10 m grids). The field observations are however valuable to assess the overall
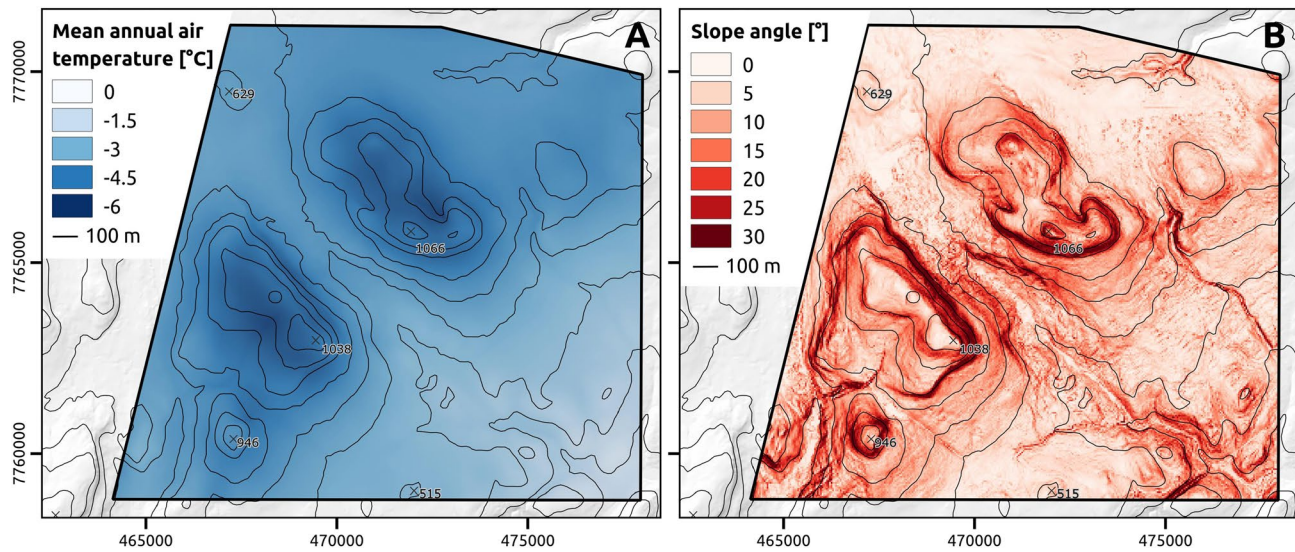
Figure 4. Spatial distribution of two explanatory variables. (a) Mean annual air temperature (MAAT) (Aalto et al., 2017). (b) Slope angle (NMA, 2016; Porter et al., 2018). Similar maps for the five other selected variables (Table 2) are shown in Supplement (Figure S4).

consistency of the InSAR spatial patterns at the landscape scale. Additional visual interpretation has been performed using 0.25–0.5 m resolution orthophotos from summer 2010, 2016, and 2018 (NMA, 2020b).

3.3. Environmental Data as Explanatory Variables

Seven environmental datasets, used as explanatory variables, were related to the InSAR products (response variables). The explanatory variables represent the climatic, geomorphic, hydrological and biological conditions in the study area (Table 2).

Climatic variables include the mean annual air temperature (MAAT) based on air temperature modeled from 942 climate stations in Scandinavia between 1981 and 2010 (Aalto et al., 2017) (Figure 4a) and the snow cover duration (SCD) using 1984–2016 Landsat-5, -7, and -8 imagery (Niittynen & Luoto, 2018; Niittynen, Heikkinen, et al., 2018). InSAR does not document the winter period and the pixels persistently covered by snow. However, variable duration of seasonal snow cover prior to InSAR measurements leads to variable meltwater input and impacts the thermal transfer between the atmosphere and the ground.

Geomorphic variables include the slope angle based on the ArcticDEM (Porter et al., 2018) and the Norwegian DEM (NMA, 2016) (Figure 4b), as well as two surface geology variables. The Norwegian DEM (original resolution 10 m) was used to fill missing data in the ArcticDEM mosaic (∼5% of the study area) by bilinearly interpolating the Norwegian DEM to match with the ArcticDEM original resolution (1.857 m) and aggregating the merged product by a factor of six resulting in a final ∼11 m DEM (Niittynen et al., 2020). Surface geology variables were extracted from a 2 m resolution land cover map based on field surveys and optical images (resolution 0.5–1.4 m) (Niittynen & Luoto, 2018), documenting the distribution of six classes: water bodies, fluvial deposits, moraines, bedrock, boulder fields, and peat material (Supplemental Figure S4). The binary dataset has been transformed to continuous by calculating the number of 2 m pixels inside 40 m pixels. The resulting values represent the percent (0%–100%) of the material covering the pixel surface. In order to reduce model complexity and overfitting potential, we included only two surface geology variables, hereafter referred to as Peat and Boulder (Table 2). The selection was based on the decrease in explained deviance by the models when each variable was omitted in their turn from a model containing all variables. Based on averaged deviance reductions over 10 permutations for each modeling technique (see Section 3.4) and the three InSAR responses, Peat and Boulder had the highest statistical contributions.

Hydrological and biological variables include the topographic wetness index (TWI) computed in SAGA GIS (System for Automated Geoscientific Analyses; Conrad et al., 2015) and the pixel-wise 95% quantile of the normalized difference vegetation index (NDVI) computed from 97 mostly cloud-free Sentinel-2 images
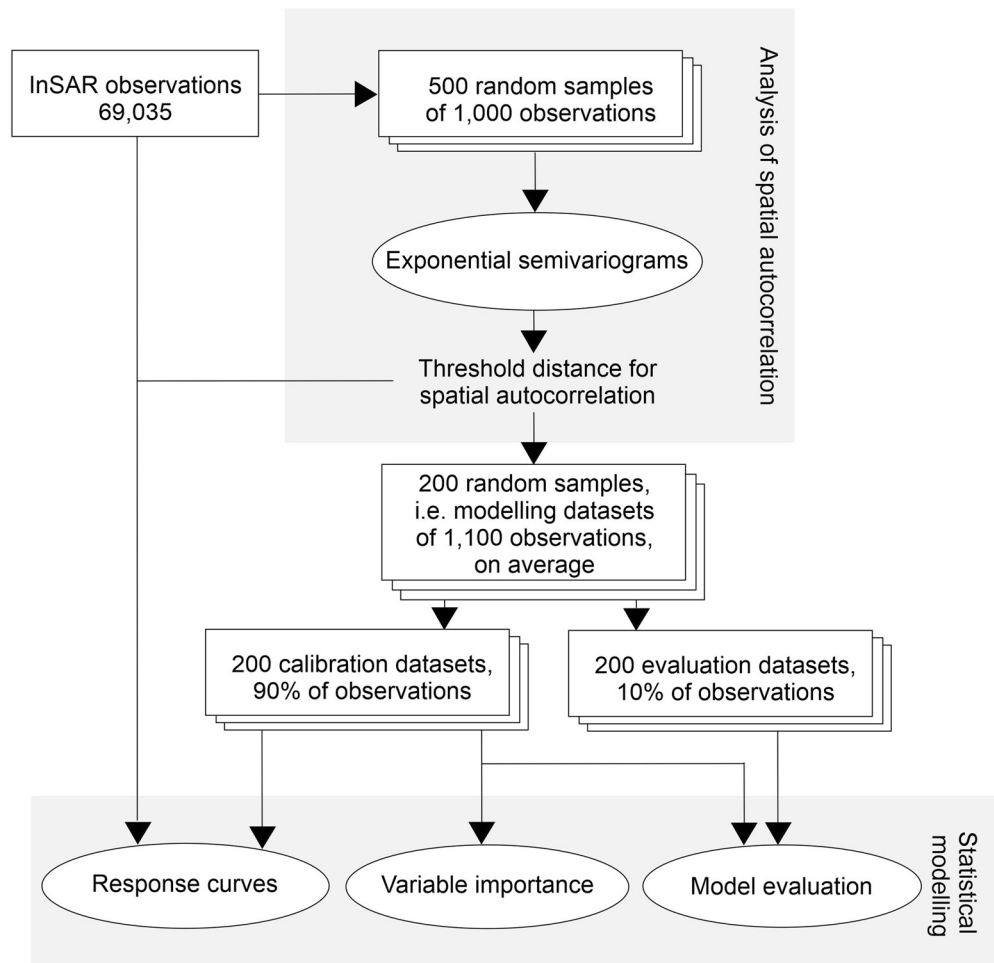
Figure 5. Schematic illustration of the statistical modeling workflow.

June–September 2016–2019. Pixels with adverse conditions (deep shadows, snow, water, or clouds) were masked out prior to calculating the quantiles. The 95% quantile was selected over the pixel-wise maximum to further limit the possible effects of erroneous pixel values.

All the variables (Table 2) were resampled to 40 m pixel resolution using the "Resample" function in ArcGIS 10.7.1 (ESRI, 2019) with bilinear sampling to spatially match with InSAR results. After removing pixels with no data, there were 68,590 pixels documented both by the InSAR products (response variables) and the environmental data (explanatory variables). Maps showing the spatial distribution of SCD, NDVI Peat, Boulder, TWI are in Supplement (Figure S4). The distributions of all variable values are shown in Supplement (Figure S5).

3.4. Explanatory Statistical Modeling

We used statistical modeling to examine the importance and effect of the selected environmental factors on InSAR mean annual ground velocities. The model inputs and outputs are floating velocity values expressed in mm/yr. The modeling was conducted with the R Statistical Software (R-version 3.6.3). Prior to modeling, we explored bivariate Spearman correlations in the modeling dataset (Supplemental Figure S6). Only the correlation between MAAT and NDVI (0.70) reached the usually applied |0.70| threshold for multicollinearity (Dormann et al., 2013). We additionally applied variance inflation factor (VIF) analysis to test whether multicollinearity between the explanatory variables was confounding the modeling. VIF values for each variable were <6, which is under the critical threshold value of 10 (Dormann et al., 2013). This suggests
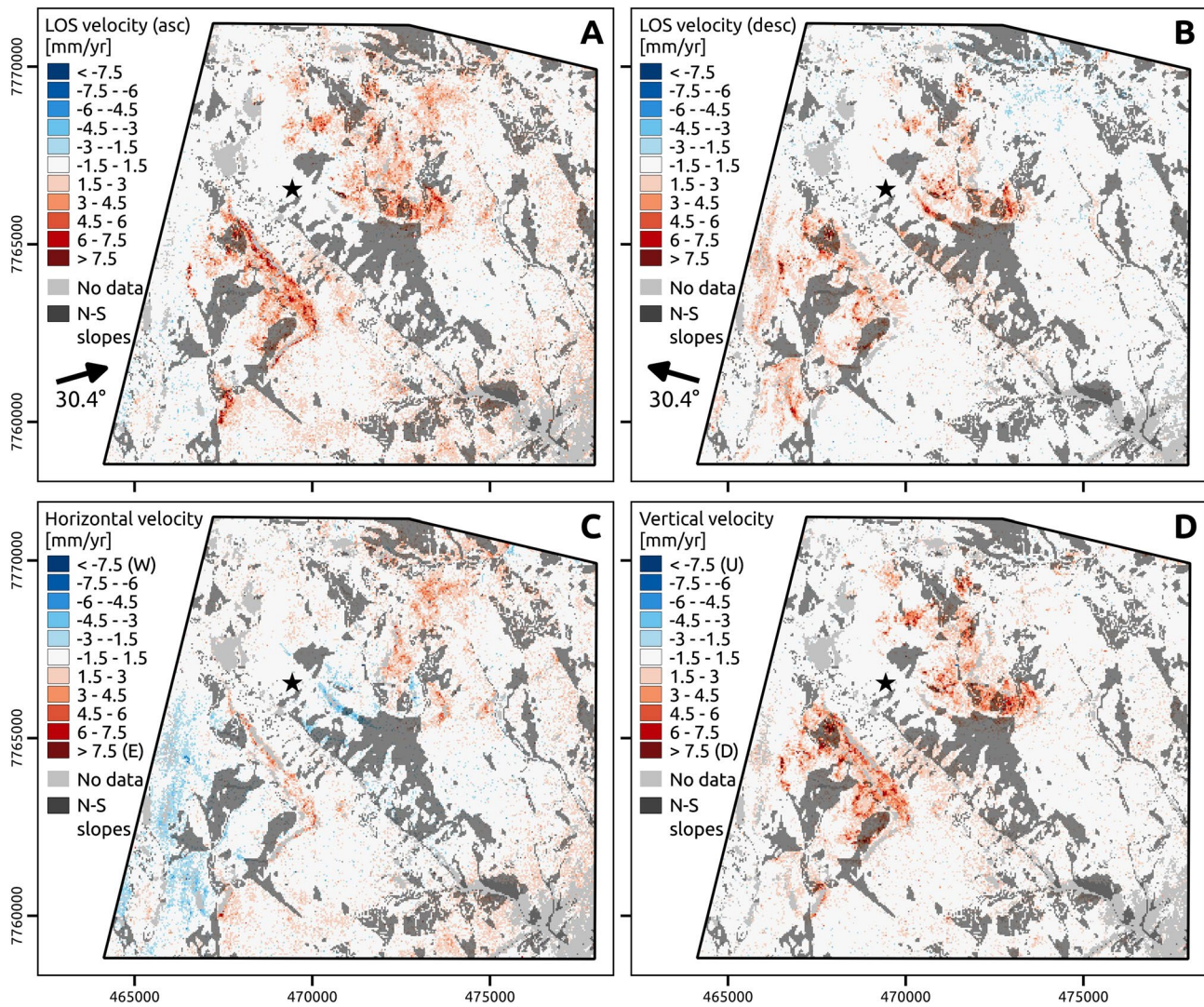
Figure 6. Initial InSAR datasets. (a and b) Mean annual ground velocity maps along the line-of-sight (LOS). Black arrows show the LOS orientations (the labels indicate the incidence angles). Negative values indicate a decrease of the sensor-to-ground distance, positive values an increase of the sensor-to-ground distance. (a) Velocity [mm/yr] along the ascending (asc) LOS. (b) Velocity [mm/yr] along the descending (desc) LOS. (c and d) Directional velocity after 2D decomposition. (c) Horizontal East–West velocity. Negative values: toward West (W). Positive values: toward East (e). (d) Vertical Up–Down velocity. Negative values: upwards (U). Positive values: downwards (d). Black star: InSAR reference point. Semi-opaque dark gray layer: areas masked out in further analysis (North-/South-facing slopes, see Section 3.1).

that strong multicollinearity is not present in the dataset. The three InSAR products (see Section 3.1) are examined separately as response variables: 1) the horizontal velocity, 2) the vertical velocity, and 3) the combined 2D velocity.

In order to account for the potential uncertainties related to single models, we used four techniques. The generalized boosting method (GBM, R package dismo; Elith et al., 2008) is the main method used to discuss the findings, while three others are applied to assess the results' consistency (Supplement Text S0). GBM was run with a learning rate of 0.001, a bag fraction of 0.75, and a tree complexity of 5 (Elith et al., 2008). A slow learning rate was chosen to ensure that single trees would not have an overly high contribution to the final model. We also made sure that 1,000 trees at minimum and 3,000 trees at maximum were fitted and used the gbm.step function (Elith et al., 2008) to determine the optimal number of trees in order to minimize holdout deviance.

Table 2
List of Explanatory Variables and Properties of the Initial Datasets

Name	Description	Unit	Data source	Native resolution [m]	References
MAAT	Mean annual air temperature	°C	Weather stations and topo-climatic modeling	10 m	Aalto et al. (2017)
SCD	Snow cover duration	Days	Landsat-5, -7, and -8	30 m	Niittynen, Heikkinen, et al. (2018) and Niittynen and Luoto (2018)
Slope	Slope angle	Degrees	ArcticDEM and Norwegian Mapping authority	11.142 m	Porter et al. (2018) and NMA (2016)
Peat	Surface geology class "Peat"	Unitless (%[a])	Pleiades imagery	2 m	Niittynen and Luoto (2018)
Boulder	Surface geology class "Boulder"	Unitless (%[a])	Pleiades imagery	2 m	Niittynen and Luoto (2018)
TWI	Topographic wetness index	Unitless	ArcticDEM and Norwegian Mapping authority	11.142 m	Böhner et al. (2002), Conrad et al. (2015), and NMA (2016)
NDVI	95% quantile of normalized difference vegetation index	Unitless	Sentinel-2	10 m	Rouse et al. (1974)

Abbreviations: MAAT, mean annual air temperature; NDVI, normalized difference vegetation index; SCD, snow cover duration; TWI, topographic wetness index.
[a]Unit after binary to continuous transformation.

The models were fitted using all the selected seven environmental variables (see Section 3.3) in order to allow comparisons between variable contributions for each response. The procedure follows the workflow illustrated in Figure 5. In total, the InSAR mapping yielded 69,035 pixels across the study area. The high density of measurements can lead to a problem of spatial autocorrelation, that is, nearby observations are likely to be more similar with each other than those further away (Legendre, 1993). Spatial autocorrelation can affect modeling by overfitting some random spatial patterns in variables and underestimating prediction errors. It may produce unrealistic responses and increase Type I errors in statistical testing, that is, a variable is selected to the model even if it should not be (false positive) (Dormann et al., 2007). To ensure that the spatial autocorrelation is not causing bias to model estimates, we first selected 500 random samples of 1,000 InSAR pixels and fitted exponential variograms to average semi-variances calculated from the prediction residuals of a generalized additive model based on the entire dataset (Supplements Text S0 and S7). Among the three responses, the average distance at which spatial autocorrelation dissipated was 289 meters. We then used this distance to select 200 random samples, that is, modeling datasets, from all InSAR measurements using the "Create random points" tool in ArcMap (ESRI, 2019). Thereby, on average 1,110 pixels were selected in each dataset with distributions similar to that of all InSAR measurements (Supplemental Figure S8).

Model evaluation was performed by using 90% of the spatially independent InSAR pixel values in each modeling dataset to calibrate the models and the remaining 10% to evaluate their performance. A high calibration proportion was used to maximize the representativeness of the calibration datasets of all InSAR observations. Based on the 200 runs, we computed means and confidence intervals of coefficient of determination (R^2, i.e., the proportion of explained variance), root mean square error (RMSE, in mm) and mean absolute error (MAE, in mm).

The relative importance of each environmental variable in the models was estimated by calculating a measure of variable importance (Thuiller et al., 2009). The variable importance value is the inverse Pearson's correlation between predictions that are produced with the previously calibrated models for two distinct datasets; one with intact seven variables, and another where one variable is randomized:

$$\text{Variance importance } = 1 - r\left(\text{Prediction}_{\text{intact variables}}, \text{Prediction}_{\text{one variable randomized}}\right) \qquad (1)$$

where r is the Pearson product-moment correlation. The closer the variable importance is to 1, the higher its individual contribution to predicted velocity. Each modeling technique was run using the 200 modeling datasets for each response with each variable randomized separately.

Lastly, we plotted response curves based on GBM results averaged over the 200 runs. We used the calibrated 200 models to predict the InSAR velocities for the 68,590 common pixels, in which each explanatory variable in turn was kept intact while the others were fixed to their mean. This way, we obtained 200 values depicting the response of the velocity components to each realized value of an explanatory variable over the entire range of the InSAR velocities. We then computed the average and standard deviation of these 200 values to plot response curves for each variable across their range in the entire dataset.

4. Results

4.1. InSAR Results

The initial InSAR results along LOS from both the ascending and descending geometries show expected velocities toward the sensor on slopes facing the radar, and away from the sensor on back-facing slopes (Figures 6a and 6b). Pixels with no data correspond to areas with radar layover or shadow due to steep topography, forested areas in the south-eastern part, lakes/ponds or persistent snow (InSAR coherence under the chosen threshold, see Section 3.1). Ascending and descending SBAS results are compared to the PSI maps from the InSAR Norway mapping service (see Section 3.1). Similar velocity ranges (mm/yr to cm/yr) and spatial distribution are found (Supplemental Figure S9), which can be considered as an indicator of the results' validity.

After 2D InSAR calculation and decomposition, the results show that the vertical and horizontal components of the velocity are differently distributed. On slopes, mass wasting processes lead to a combination of horizontal and vertical velocities, while the flat areas are affected by vertical velocities, especially on mountain tops (Figures 6c and 6d). Before conversion to absolute values, we analyze the relevance of the directional patterns for both the horizontal and vertical components. The average velocity at the InSAR reference point (black star in Figures 5 and 6) is −0.23, 0.20, and 0.30 mm/yr for the horizontal, vertical and 2D velocity, respectively. As expected, westwards horizontal velocities (negative values) are located on west-facing slopes, while eastwards (positive values) are on east-facing slopes (Figure 6c). Horizontal velocity has a mean of 0.44 mm/yr with a higher number of positive pixels (eastwards). This may indicate a minor shift of the velocity values due to a westward velocity at the InSAR reference point, but also represent the natural higher proportion of east-facing slopes in the area. The vertical values are mostly positive (>80%) (Figure 6d), corresponding to a subsidence, which is expected when using mean velocity measurements based on observations during the thawing periods. Among the pixels with negative (upwards) trend, over 75% are between 0 and −0.5 mm/yr and less than 1% are under −1 mm/yr. These values are part of the overall dataset variability. They are likely due to phase bias (sources introduced in Section 3.1 and further discussed in 5.3), but may also represent a natural trend.

For the exploratory statistical modeling, absolute values are considered, to focus on the movement magnitude instead of its direction. InSAR detects velocity up to 11 mm/year eastwards and westwards (horizontal component), up to 14 mm/yr vertically and up to 15 mm/yr when combining both components into a 2D information (Figure 7). The distribution is right-skewed, with clearly a higher proportion of low values (Figure 7d). Despite the low velocity in average, the results show a clear spatial pattern, with higher velocities on slopes and mountain tops (Figure 6 and S10). At the 429 locations where InSAR results overlapped with field observations (see Section 3.2), the activity rate is overall higher in areas where InSAR detected high velocities, that is, on slopes and mountain tops (Figures 7 and 8). The InSAR 2D velocity from locations rated with high activity is overall higher than those with negligible, low and medium activity (Supplemental Figure S11). Detailed maps show highly active areas where patterned ground (Figures 8a–8f) and solifluction lobes (Figures 8b–8e, 8g, and 8h) can be seen on aerial imagery.
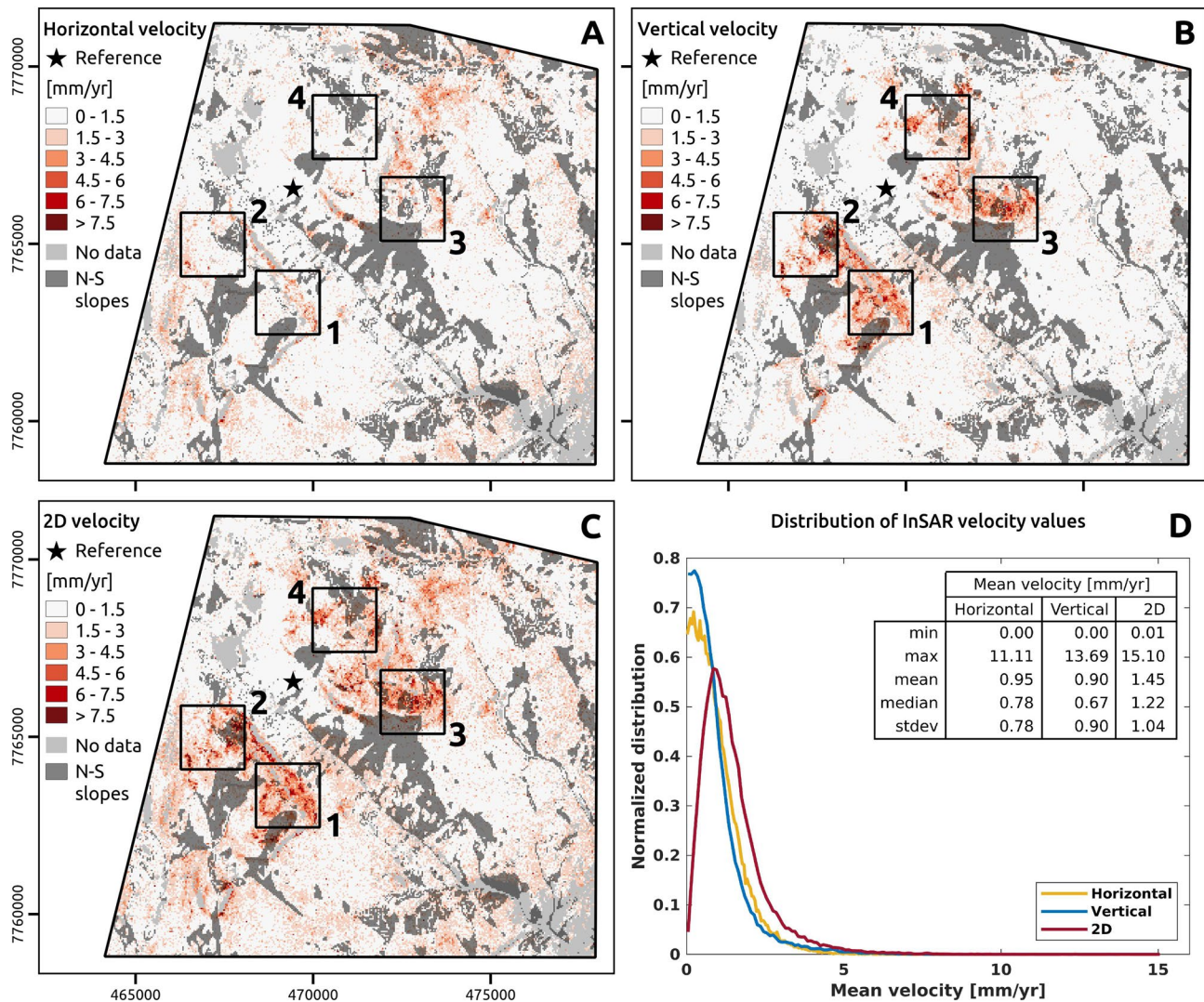
Figure 7. Absolute 2D InSAR mean annual ground velocity results used as response variables. (a) Horizontal component of the velocity [mm/yr]. (b) Vertical component of the velocity [mm/year]. (c) 2D combined velocity [mm/year]. (a–c) Black star: InSAR reference point. Semi-opaque dark gray layer: areas masked out in further analysis (North-/South-facing slopes, see Section 3.1). Black squares: detailed areas shown in Figure 8. (d) Distribution (kernel densities) and statistics of the response variables: horizontal, vertical and 2D combined velocity for the 69,035 available InSAR pixels.

4.2. Statistical Modeling

GBM results highlight contrasted model performance (Table 3). The model performed better based on the vertical component (47% of the explained variance), compared to the horizontal component (24% of the explained variance). Prediction errors for each velocity component were slightly higher for evaluation datasets and the variations explained by the models decrease sharply when predicted over independent evaluation datasets. The modeling datasets have similar distributions compared to the 69,035 InSAR measurements shown in Figure 7d (Supplemental Figure S8).

On average, Slope and MAAT (Figure 4) are the most important variables contributing to the variation of InSAR velocity (Figure 9a). Clear differences between the responses are visible. Horizontal velocity depends foremostly on slope angle, while MAAT exerts the highest influence on vertical velocity. NDVI and SCD have also notable importance, but dissimilar effects on the horizontal and vertical components. Horizontal velocity is more affected by SCD than vertical velocity, which is more influenced by NDVI. Considering the 2D velocity, which combines the horizontal and vertical components, MAAT, Slope and NDVI can be
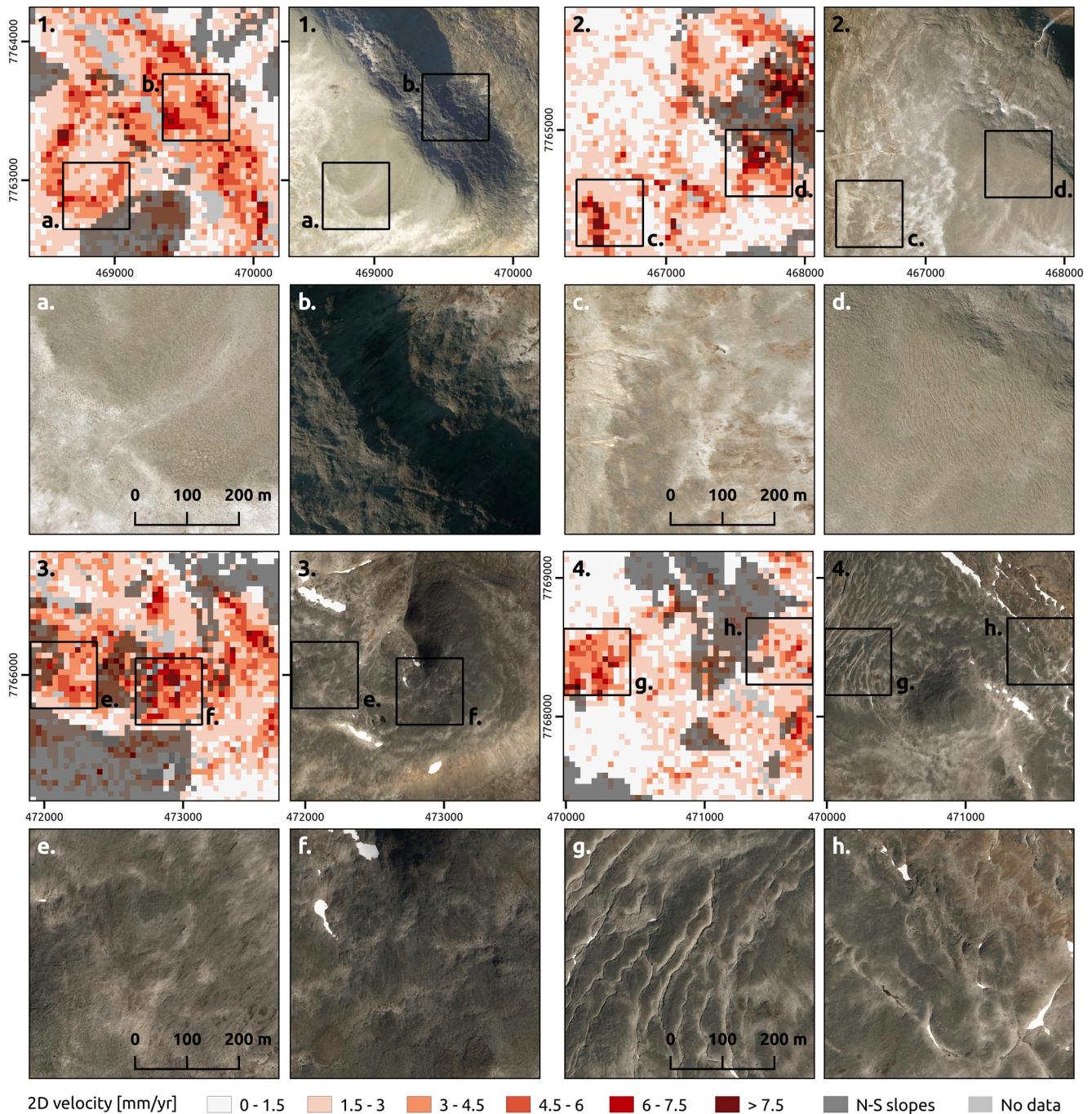
Figure 8. Detailed areas comparing 2D InSAR mean annual ground velocity (see locations 1–4 in Figure 7) and aerial orthoimagery (NMA, 2020b). a–h: Orthophoto view at a smaller extent with visual expression of cryoturbation (a, d, f) and solifluction (b, c, e, g, h) features (patterned ground and solifluction lobes) associated with the detected velocities.

retained for their importance. Despite its importance for the horizontal component, SCD has lower relative significance for the combined 2D velocity. The importance of the remaining variables (Peat, TWI, and Boulder) is low (<0.1) for all responses, albeit all three variables present a higher influence on the horizontal component. The three complementary modeling methods (Supplementary Text S0) yield similar relative importance values among the variables (Supplemental Figure S13).

Table 3

Generalized Boosting Method (GBM) Modeling Performance in Terms of Coefficient of Determination (R^2), Root Mean Square Error (RMSE) and Mean Absolute Error (MAE) and for Each Response Variable

	R^2		RMSE		MAE	
	Calibration	Evaluation	Calibration	Evaluation	Calibration	Evaluation
Horizontal	0.24 ± 0.04	0.08 ± 0.08	0.68 ± 0.03	0.74 ± 0.10	0.52 ± 0.02	0.56 ± 0.05
Vertical	0.47 ± 0.04	0.28 ± 0.13	0.66 ± 0.03	0.75 ± 0.13	0.47 ± 0.02	0.51 ± 0.05
2D	0.38 ± 0.04	0.21 ± 0.10	0.82 ± 0.04	0.90 ± 0.13	0.60 ± 0.02	0.65 ± 0.06

Note. The values (averages ± one standard deviation) are based on 200 resampling rounds for calibration (90% of observations in each sample) and evaluation datasets (10%). Evaluation results for the three complementary models are listed in Figure S12.

The response curve for the slope angle (Figure 9b) shows that it has a positive influence on the velocity, with a clear increase when slope angle exceeds 10°. Despite the difference of importance (higher for the horizontal component), the shape of the curve is similar for the three responses. The relationship between MAAT and the mean velocity is also nonlinear but more ambiguous: the vertical velocity tends to decrease with higher MAAT values, while the horizontal velocity is highest where MAAT is around −2°C. The response curve for the 2D velocity highlights the combined effect of the two previous elements, influencing differently the horizontal and vertical components. NDVI has a U-shaped response with the vertical and 2D components; the velocity tends to increase where NDVI is either lowest (<0.2) or highest (>0.6). SCD response curve shows the clearest trend for the horizontal component, with a positive impact of snow coverage duration on the velocity.
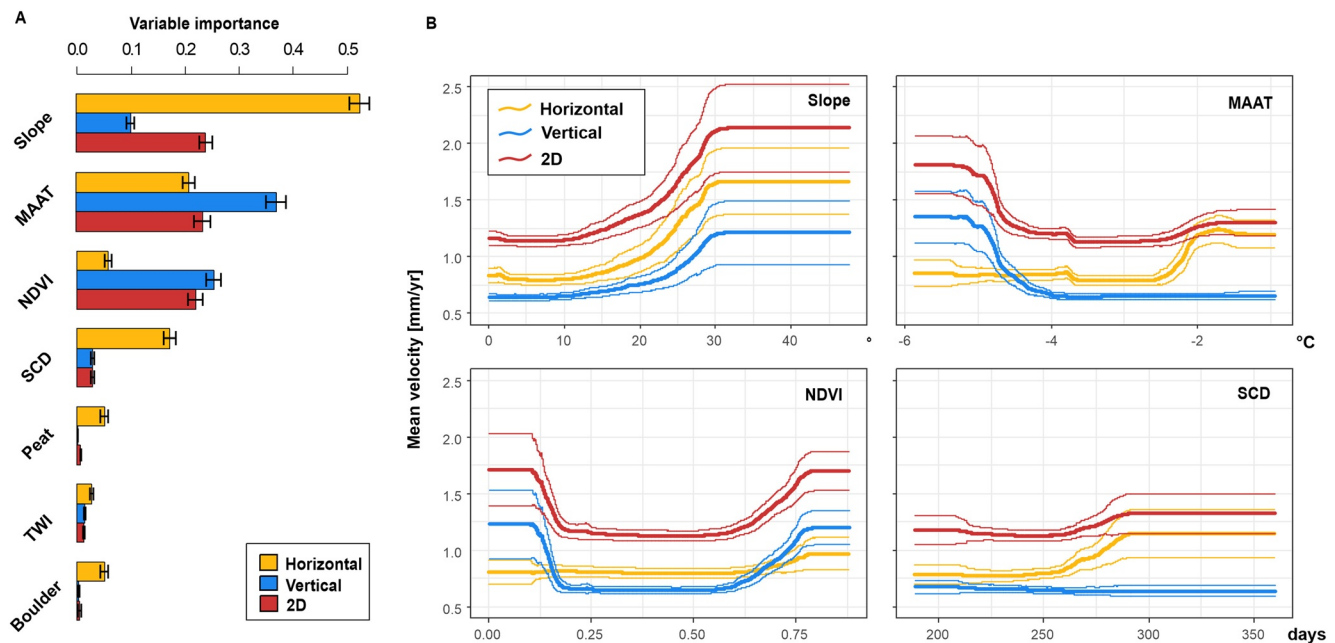
Figure 9. Variable importance and response curves based on generalized boosting method (GBM). (a) The bars represent the mean relative importance of the seven environmental variables over 200 resampling rounds and the whiskers depict the 95% confidence intervals. Variables are ordered based on their average importance for the three velocity components. (b) Response curves depict the modeled mean annual ground velocity (Y-axis) across the range of variables values in their original scale (X-axis). Thin curves represent one standard deviation from average response over 200 permutations. Response curves for the three least important variables are presented in Supplemental Figure S14. The acronyms refer to mean annual air temperature (MAAT), normalized difference vegetation index (NDVI), snow cover days (SCD), and topographic wetness index (TWI).

5. Discussion

5.1. Ground Dynamics in Rásttigáisá-Geaidnogáisá Area

The combined 2D InSAR product indicates values up to 15 mm/year. Ground dynamics in the study area is spatially variable, with higher velocities on slopes and mountain tops. The detected ground velocity is assumed to be primarily associated with cryoturbation and solifluction processes considering the periglacial context, the field and orthophoto observations (Figures 3 and 8), the low velocities (Figures 6 and 7) and the sloping but gentle topography (predominantly <30° slope angle, Figures 1 and 4b). The presence of rockslides and deep-seated gravitational slope deformation has to our knowledge not been documented in the area but can nevertheless not be excluded. Surface run-off, erosion and transport of weathered material by meltwater on steep slopes may also have a local significance.

Ground ice formation and melting associated with active layer freeze and thaw leads to frost heave and thaw subsidence (Morgenstern & Nixon, 1971; Rempel, 2007). The cryoturbation activity is typically associated with differential movement due to the variability of the frost-susceptibility and the ground water content (Peterson & Krantz, 2008; Van Vliet-Lanoë, 1991; Wilson & Sellier, 1995). Although complex mixing and convection are known to have a significant impact on the dynamics of cryoturbated ground and the re-distribution of organic material (Bockheim, 2007; Van Vliet-Lanoë, 1991), these subsurface mechanisms are expected to have a negligible effect in this study due to the surface measurements. Small magnitude and heterogenous deformation over small surfaces are in addition likely to remain undetected when documenting ground velocities with 40 m resolution InSAR pixels. The InSAR results emphasize the downward component of the cryoturbation due to the use of SAR images during the thawing seasons. Millimetric to centimetric seasonal amplitude is in the expected range in mountainous and subarctic areas, characterized by discontinuous permafrost, thin fine-grained unconsolidated deposits and low ice content (Gruber, 2020; Matsuoka et al., 2003; Smith, 1987). In this study, however, the seasonal component is underestimated due to the use of mean annual products.

Solifluction is the dominant process (Figure 3) due to the sloping terrain of the study area (Figures 1 and 4b). Solifluction combines the effect of the needle ice and frost creep (heave normal to the inclined surface followed by vertical settlement) and the gelifluction (shear deformation associated with water content from the seasonal thawing of ground containing excess ice) (Harris et al., 1997; Harris & Davies, 2000; Harris, Kern-Luetschg, et al., 2008; Matsuoka, 2001). The net movement is downslope, which explains why 2D InSAR detects a combination of horizontal and vertical components in these areas. Millimetric to centimetric solifluction annual rate (net downslope velocities) is in the range of subarctic areas and mid-latitude mountainous regions with seasonal frost or warm permafrost conditions (Ballantyne, 2013; Harris, Kern-Luetschg, et al., 2008; Matsuoka et al., 1997; Ridefelt et al., 2009). Decimetric to metric annual rates have also been reported but are generally associated with high frequency freeze-thaw cycles or deep freeze-thaw penetration in fine frost-susceptible material (Matsuoka, 2001).

At the regional scale, the results show that InSAR is valuable in studying the distribution of the ground velocity over large areas and locating the most active parts of the landscape, at a scale and resolution hard to achieve by other techniques. However, as also discussed by other studies (Daout et al., 2017; Eckerstorfer et al., 2018; Eriksen, Lauknes, et al., 2017; Reinosch et al., 2020; Rouyet et al., 2019), relating these measurements to actual processes to further interpret their controls is the major scientific challenge of the exploitation of InSAR technology in periglacial environments. The ground type (grain size influencing the frost susceptibility), the ground moisture, the topography and the snow/vegetation distribution have an impact on the local variability of movement magnitude but the respective influence of each factor is still not fully understood. This is why the combination of InSAR and statistical modeling can positively contribute to further understand the links between ground dynamics and environmental conditions.

5.2. Factors Controlling InSAR Ground Velocity

The Slope and MAAT variables (Figure 4) are the key factors contributing to the spatial variability of the ground velocity, but they have different importance and effects on both components of the 2D mean velocity (Figure 9). The high importance of slope angle for the horizontal component matches the theoretical

expectation that the solifluction rate increases with the slope inclination (Harris et al., 1997; Matsuoka, 2001). However, the response curves indicate that there is an upper limit for the effect, as just under 30° the curves begin to flatten. This suggests that steeper slopes are less favorable for solifluction occurrence (Matsuoka, 2001). Too steep slopes do not allow for thick layer of soil to hold, and may lead to high water drainage and little snow accumulation, detrimental for solifluction to occur (Matsuoka, 2001). A similar leveling off effect has been found by Hjort and Luoto (2011) and Hjort et al. (2014) who showed good concordance with hypothetical response curves. It should be noted, however, that the flat curves after ∼32° are also affected by the relatively small amount of observations in the randomly sampled modeling datasets, as suggested by the distribution of the values in all available InSAR pixels (Supplemental Figure S5). The air temperature is the second most important factor, controlling primarily the vertical component of the ground velocity (Figure 9a). Interestingly, the response curves show that MAAT has a two-sided effect, impacting the two velocity components differently (Figure 9b). For the vertical component, the negative relationship suggests that low temperatures in the high-altitude parts of the study area promoting frost action, which concurs with conclusions from Hjort (2014). For the horizontal component, the relationship is nonlinear and positive. This seems reasonable as well-developed soils including fine sediments promote solifluction at low altitudes characterized by relatively high MAAT. Frost-susceptible silt-rich soils are typically expected to be more favorable to frost creep (Harris et al., 1995). The peak of horizontal velocity in areas with MAAT around −2°C (Figure 9b) likely represents the footslopes that include a relatively large horizontal component due to solifluction in low-inclined terrain. Longer thawing seasons and warmer ground conditions also tend to increase the amount of liquid water into the ground and promote the gelifluction component of the solifluction. Low temperatures may delay and decrease the length of the thawing season, thus decreasing the solifluction activity. It concurs with other studies showing that solifluction rates increase with higher MAAT (Matsuoka, 2001; Ridefelt et al., 2009).

Despite their more ambiguous importance and effects, NDVI and SCD have notable contributions in the models. NDVI mostly influences the vertical component (Figure 9a). The response curve shows a nonlinear and complex relationship (Figure 9b), indicating that sparsely vegetated surfaces (typically rocky terrain at high-altitude) tend to be associated with high velocities recorded at the tops and upper slopes of the mountains in the areas affected by subsidence. Solifluction lobes at the mountain footslopes are covered by low vegetation to a varying degree. Near the mountain tops, only lichen is found on rocky surfaces while the underlying finer material is sparsely or not vegetated. The effect of the vegetation on the velocity is in line with the MAAT and partly related to their high mutual correlation. Both variables reflect the prominent altitudinal gradient in the study area (>900 m), which strongly controls the preconditions for frost activity. However, NDVI also allows for examining additional indirect factors affecting ground movement. High NDVI can indeed be associated with high velocity, a positive effect visible both on the response curves for the vertical and horizontal components. The two-sided and apparently contradictory relationship between vegetation cover and periglacial processes have also been discussed in previous studies related to cryoturbation and solifluction activity. Peterson et al. (2003) show that vegetation cover may have a constraining effect on cryoturbation, especially in the presence of insulative plant communities. The biogeomorphic model on solifluction lobes from Eichel et al. (2017) also highlights that dense vegetation acts to stabilize the ground. On the other hand, high NDVI coincides with areas where the soil is well-developed allowing for cryoturbation and solifluction to occur due to water accumulation and fine-grained frost-susceptible sediments. Earth or turf hummocks showing strong frost action can for example, be covered by abundant low-stature vegetation (Grab, 2005; Kojima, 1994). On solifluction lobes, Eichel et al. (2017) showed that vegetation growing in wet areas can be associated with high amplitude of cryotic deformation. Positive relationship between NDVI and solifluction are similarly found in Ridefelt et al. (2009, 2010) and Hjort et al. (2014). The presence of vegetation may also influence the snow distribution, leading to variable water content and thus promoting differential frost heave (Daanen et al., 2008; Nicolsky et al., 2008). In general, as discussed by Hjort (2014) and Hjort and Luoto (2009), the vegetation is mostly an indirect factor for periglacial activity and encompasses a variety of species with different habits, which can have contrasting impacts on ground stability. This complexity may explain the ambiguous relationship with the response variables. It should also be noted that the positive effect of high NDVI to the vertical component can also correspond to an artifact. Even in areas where the InSAR coherence is over the chosen threshold, scattering mechanisms related to herbaceous vegetation may affect the results (Ansari et al., 2020). Birefringence through the

plant elements, phenological and interannual variations in plant height may lead to biased displacement estimates (Zwieback & Hajnsek, 2014). SCD positively influences the horizontal component (Figure 9b). This concurs with conclusions from several studies, showing that uneven distribution of snow leads to differential ground movement and melting of prolonged snow patches raises the ground moisture content of the thawed layer, which promotes gelifluction (Jaesche et al., 2003; Matsuoka, 2001). Early and deep snow patches can also prevent ground freezing in nivation hollows and provide entry points for groundwater seepage further downslope (Harris, Kern-Luetschg, et al., 2008).

Considering the conclusions of other studies about the controls of cryoturbation and solifluction processes, the low contributions of the surface geology (Peat, Boulder) and hydrological (TWI) factors may seem surprising. In this study, we hypothesize that the low importance of these variables is related to the thin and/or coarse sediment cover, little frost-susceptibility and low–medium ice content (see Sections 2 and 3.2) that lead to the low detected velocities in the area. It is also likely due to the characteristics of the products/indexes used for documenting the spatial variability of the two factors. The ground type, in terms of grain size and frost susceptibility, is expected to have an impact on the movement amplitude (Konrad, 1999; Van Vliet-Lanoë, 1991). However, the variables Peat and Boulder are based on relatively coarse products (Figure S4) that do not fully allow for documenting the frost susceptibility at the resolution of the analysis. Similarly, water availability is expected to contribute to the differential distribution of frost-related ground movement (Harris et al., 1995; Hjort, 2014; Jaesche et al., 2003). The fact that TWI has a negligible importance may indicate that this index is not the most adapted at the considered resolution despite its documented potential in explaining measured fine-scale (1 m^2) variability of soil moisture in a similar sub-arctic environment (Kemppinen et al., 2018). In the context of ground dynamics, this could be because TWI is a purely topographically-based surface water distribution index that does not consider soil properties, influencing infiltration or runoff conditions, as well as ground ice formation. These elements show the challenge of studying ground freeze-thaw processes due to the highly variable water content, ice and sediment distribution at very fine-scale; an issue that has been further discussed in several other studies (Cable, et al., 2018; Gruber, 2020; Schuh, et al., 2017; Shiklomanov et al., 2010). It highlights the need for including alternative data in future studies and considering the properties of the ground material to document the effective significance of soil moisture on ground movement.

In general, the limitation of a potential scale discrepancy must be considered when considering any geoscientific study based on remote sensing. Low to medium resolution satellite products have the advantage to document large areas with near-continuous coverage, but the drawback of averaging information at a scale that is, not fully representative. The conclusions about the relative spatial variability of the measurements and their relations with environmental variables at similar resolution are valid, but inferred links between remotely sensed measurements and ground processes must always be treated carefully.

5.3. InSAR and Statistical Modeling: Potential and Limitations

We acknowledge that due to the low magnitude of the InSAR velocities and the right-skewed distribution of the values, the results are sensitive to small bias of displacement estimates. The main InSAR error sources are 1) the uncorrected atmospheric effects (Zebker et al., 1997); 2) the bias due to changes of surface properties and their effects on scattering mechanisms, in relation with snow, moisture and vegetation (De Zan et al., 2014; Zwieback et al., 2015, 2016; Zwieback & Hajnsek, 2014); and 3) a potential shift of the velocity due to a wrong assumption of stability at the location of the reference point (Antonova et al., 2018). The procedure to mitigate these three elements have been presented in Section 3.1 and we estimated that the accuracy is below 1 mm/yr (Supplemental Figure S3). It should, however, be noted that the impact of the scattering mechanisms on SBAS results are not fully understood yet and thus difficult to assess quantitatively. Understanding the physical sources of the potential bias and modeling the complex effects of the moisture, snow and biomass changes is a dedicated on-going research topic (Ansari et al., 2020). It should also be reminded that this study focuses on the relative spatial distribution of the ground velocities and that the use of a multi-annual averaging and a linear deformation model does not allow for documenting the seasonality of the processes. Comprehensive time series analyses should be considered in future studies combining InSAR and statistical modeling. Due to the unavailability of complementary displacement measurements in the area, this study does not provide a quantitative validation of the InSAR results. However, several

qualitative indicators have been used to assess the results' validity (see Section 4.1). First, the amplitude and distribution of the results are generally consistent with the PSI results from the InSAR Norway ground motion mapping service. Second, the spatial variability of the velocity follows expected patterns, with eastwards/westwards horizontal velocities on respectively east- and west-facing slopes, and with higher velocities on slopes and mountain tops. This is overall consistent with field observations of the cryoturbation and solifluction activity. Third, results from 2D InSAR calculation do not show any major shift of the velocity indicating that the choice of the InSAR reference point was adapted.

The relatively low model performance (Table 3) in this study can be explained by a) the overall low magnitude of ground movement across the area; b) the complex and indirect relation between environmental variables and the ground velocities, as well as the scale discrepancy between measurements and processes; and c) the relatively small number of observations in the calibration sets (on average 1,100) that may not cover the entire gradient of environmental conditions in the study area. Contrary to the previous studies applying modeling based on field-mapped processes and landforms (Hjort, 2014; Hjort & Luoto, 2009; Hjort et al., 2007), the responses here represent ground velocity regardless of the underlying processes. The unexplained variation by the models is arguably attributed to the frost susceptibility of ground material, fine-scale soil moisture, and microclimatic conditions (e.g., solar radiation, wind processes) (Aalto, Scherrer, et al., 2018), which could not be accounted for at optimal thematic or spatial resolution. A central aspect that may have affected our ability to accurately predict the mean velocity is the scale mismatch between the InSAR resolution (40 m) and the assumed ground processes (Luoto & Hjort, 2006; Walsh et al., 1998). We argue that examination of frost-related ground movement would benefit from a higher spatial resolution in both InSAR and geospatial data on environmental conditions. Our results show a notably higher amount of explained variation for the vertical component compared to the horizontal velocity. We suggest that it is more complicated to explain the horizontal component because eastwards/westwards movement can less directly be related to a specific process. A slope affected by solifluction typically includes both a vertical and a horizontal component, and flat areas are dominated by vertical patterns. While the vertical downward trend documented by the InSAR averaged measurements can be related to the melting of the ice in the seasonally thawing layer of the ground, the horizontal component is a more complex interaction of the frost action (needle ice and frost creep) and the gelifluction (shear deformation).

Despite the discussed challenges, the results of the statistical modeling of 2D InSAR measurements in Rásttigáisá-Geaidnogáisá area provide interesting insights on the environmental controls of periglacial ground dynamics. This study is a first contribution toward integrating InSAR and statistical modeling in periglacial research. Other strategies based on similar techniques could be investigated in the future. Better model performance may be reached by focusing on one previously inventoried landform type and clearer response curves may be found by selecting areas where movement magnitude is expected to be higher. The exploitation of time series can be considered to analyze the seasonal progression of the displacement. InSAR maps could also be used as a variable among others to explain the distribution of specific landforms.

6. Conclusion

We mapped mean annual ground velocity in a mountainous landscape in Northern Norway using Sentinel-1 Synthetic Aperture Radar Interferometry (InSAR). The 2D InSAR products were used as response variables in statistical modeling based on a set of seven climatic, geomorphic, hydrological and biological variables.

Based on the results, four main conclusions can be drawn:

1. The study area is affected by mm/yr to cm/yr mean annual ground velocities, with values up to 15 mm/yr. The horizontal and vertical components of the 2D velocity are distributed differently over flat areas and slopes and highlight the areas affected by active cryoturbation and solifluction.
2. The statistical models showed contrasted performance depending on the velocity component (R^2 between 0.24 and 0.47). The unexplained variance may be attributed to the low velocities, the discrepancy between the spatial resolution of the remote sensing products and the studied processes, as well as the complex relationships between environmental variables, periglacial processes and documented responses (ground velocities).

3. The slope angle and the mean annual air temperature are the key factors contributing to the spatial variability of the ground velocity in the study area. The amount of vegetation and the snow cover duration have also notable contributions in the models and are interpreted as indirect proxies of ground material and moisture conditions.

4. The relative importance of the environmental factors on both components of the 2D velocity vary significantly. The vertical velocity is mostly influenced by the air temperature and the vegetation, while the main variable controlling the variability of the horizontal component is the slope angle, followed by the air temperature and the snow coverage. These results are attributed to the different characteristics of cryoturbation and solifluction processes, operating differently over flat areas and slopes.

As a first attempt of coupling InSAR and explanatory statistical modeling in periglacial landscapes, our study highlights the potential to integrate both techniques for a better understanding of the environmental factors controlling ground dynamics and suggest novel ways to characterize extensive and hard-to-access cold environments.

Data Availability Statement

Model inputs (response and environmental variables) and outputs (calibration/evaluation model performance and predictions) are openly available. Data is available in Zenodo repository (https://doi.org/10.5281/zenodo.4173256). Additional data sources used in this study are listed in the references, included in the figures and tables, or in the Supporting Information associated with this publication.

References

Aalto, J., Harrison, S., & Luoto, M. (2017). Statistical modeling predicts almost complete loss of major periglacial processes in Northern Europe. *Nature Communications*, *8*, 515. https://doi.org/10.1038/s41467-017-00669-3

Aalto, J., Karjalainen, O., Hjort, J., & Luoto, M. (2018). Statistical forecasting of current and future circum-Arctic ground temperatures and active layer thickness. *Geophysical Research Letters*, *45*(10), 4889–4898. https://doi.org/10.1029/2018GL078007

Aalto, J., Scherrer, D., Lenoir, J., Guisan, A., & Luoto, M. (2018). Biogeophysical controls on soil-atmosphere thermal differences: Implications on warming Arctic ecosystems. *Environmental Research Letters*, *13*(7), 074003. https://doi.org/10.1088/1748-9326/aac83e

Ansari, H., De Zan, F., & Parizzi, A. (2020). Study of systematic bias in measuring surface deformation with SAR interferometry. *IEEE Transactions on Geoscience and Remote Sensing*, *59*, 1285–1301. https://doi.org/10.1109/TGRS.2020.3003421

Antonova, S., Sudhaus, H., Strozzi, T., Zwieback, S., Kääb, A., Heim, B., et al. (2018). Thaw subsidence of a Yedoma landscape in Northern Siberia, measured in situ and estimated from TerraSAR-X interferometry. *Remote Sensing of Environment*, *10*(4), 494. https://doi.org/10.3390/rs10040494

Ballantyne, C. K. (2013). A 35-year record of solifluction in a maritime periglacial environment. *Permafrost and Periglacial Processes*, *24*(1), 56–66. https://doi.org/10.1002/ppp.1761

Bamler, R., & Hartl, P. (1998). Synthetic aperture radar interferometry. *Inverse Problems*, *14*(4), R1–R54. https://doi.org/10.1088/0266-5611/14/4/001

Baran, I., Stewart, M. P., Kampes, B. M., Perski, Z., & Lilly, P. (2003). A modification to the Goldstein radar interferogram filter. *IEEE Transactions on Geoscience and Remote Sensing*, *41*(9), 2114–2118. https://doi.org/10.1109/TGRS.2003.817212

Barboux, C., Delaloye, R., & Lambiel, C. (2014). Inventorying slope movements in an Alpine environment using DInSAR. *Earth Surface Processes and Landforms*, *39*(15), 2087–2099. https://doi.org/10.1002/esp.3603

Barboux, C., Strozzi, T., Delaloye, R., Wegmüller, U., & Collet, C. (2015). Mapping slope movements in Alpine environments using TerraSAR-X interferometric methods. *ISPRS Journal of Photogrammetry and Remote Sensing*, *109*, 178–192. https://doi.org/10.1016/j.isprsjprs.2015.09.010

Bartsch, A., Leibman, M., Strozzi, T., Khomutov, A., Widhalm, B., Babkina, E., et al. (2019). Seasonal progression of ground displacement identified with satellite radar interferometry and the impact of unusually warm conditions on permafrost at the Yamal Peninsula in 2016. *Remote Sensing*, *11*(16), 1865. https://doi.org/10.3390/rs11161865

Berardino, P., Fornaro, G., Lanari, R., & Sansosti, E. (2002). A new algorithm for surface deformation monitoring based on small baseline differential SAR interferograms. *IEEE Transactions on Geoscience and Remote Sensing*, *40*(11), 2375–2383. https://doi.org/10.1109/TGRS.2002.803792

Biskaborn, B. K., Smith, S. L., Noetzli, J., Matthes, H., Vieira, G., Streletskiy, D. A., et al. (2019). Permafrost is warming at a global scale. *Nature Communications*, *10*(1), 1–11. https://doi.org/10.1038/s41467-018-08240-4

Blois, J. L., Williams, J. W., Fitzpatrick, M. C., Jackson, S. T., & Ferrier, S. (2013). Space can substitute for time in predicting climate-change effects on biodiversity. *Proceedings of the National Academy of Sciences*, *110*(23), 9374–9379. https://doi.org/10.1073/pnas.1220228110

Bockheim, J. G. (2007). Importance of cryoturbation in redistributing organic carbon in permafrost-affected soils. *Soil Science Society of America Journal*, *71*(4), 1335–1342. https://doi.org/10.2136/sssaj2006.0414N

Boeckli, L., Brenning, A., Gruber, S., & Noetzli, J. (2012). Permafrost distribution in the European Alps: Calculation and evaluation of an index map and summary statistics. *The Cryosphere*, *6*(4), 807–820. https://doi.org/10.5194/tc-6-807-2012

Böhner, J., Köthe, R., Conrad, O., Gross, J., Ringeler, A., & Selige, T. (2002). Soil regionalization by means of terrain analysis and process parameterisation. In E. Micheli, E. F. Nachtergaele, & L. Montanarella (Eds.), *Soil classification 2001* (pp. 213–222), Research Report No. 7, EUR 20398 EN. Luxembourg: European Soil Bureau.

Bonnaventure, P. P., & Lamoureux, S. F. (2013). The active layer: A conceptual review of monitoring, modeling techniques and changes in a warming climate. *Progress in Physical Geography*, Vol. *37*(3), 352–376. https://doi.org/10.1177/0309133313478314

Brown, J., Ferrians, O., Heginbottom, J. A., & Melnikov, E. (2002). *Circum-arctic map of permafrost and ground-ice conditions, version 2.* Boulder, Colorado, USA: National Snow and Ice Data Center (NSIDC). https://doi.org/10.7265/skbg-kf16

Cable, S., Elberling, B., & Kroon, A. (2018). Holocene permafrost history and cryostratigraphy in the High-Arctic Adventdalen Valley, central Svalbard. *Boreas*, *47*(2), 423–442. https://doi.org/10.1111/bor.12286

Cavalié, O., Doin, M. P., Lasserre, C., & Briole, P. (2007). Ground motion measurement in the Lake Mead area, Nevada, by differential synthetic aperture radar interferometry time series analysis: Probing the lithosphere rheological structure. *Journal of Geophysical Research: Solid Earth*, *112*(B3), B03403. https://doi.org/10.1029/2006JB004344

Chen, C., & Zebker, H. A. (2002). Phase unwrapping for large SAR interferograms: Statistical segmentation and generalized network models. *IEEE Transactions on Geoscience and Remote Sensing*, *40*(8), 1709–1719. https://doi.org/10.1109/TGRS.2002.802453

Chen, J., Wu, Y., O'Connor, M., Cardenas, M. B., Schaefer, K., Michaelides, R., & Kling, G. (2020). Active layer freeze-thaw and water storage dynamics in permafrost environments inferred from InSAR. *Remote Sensing of Environment*, *248*, 112007. https://doi.org/10.1016/j.rse.2020.112007

Christiansen, H. H., Etzelmüller, B., Isaksen, K., Juliussen, H., Farbrot, H., Humlum, O., et al. (2010). The thermal state of permafrost in the nordic area during the international polar year 2007–2009. *Permafrost and Periglacial Processes*, *21*(2), 156–181. https://doi.org/10.1002/ppp.687

Conrad, O., Bechtel, B., Bock, M., Dietrich, H., Fischer, E., Gerlitz, L., et al. (2015). System for automated geoscientific analyses (SAGA) v. 2.1.4, *Geoscientific Model Development 8*, 1991–2007. https://doi.org/10.5194/gmd-8-1991-2015

Daanen, R. P., Misra, D., Epstein, H., Walker, D., & Romanovsky, V. (2008). Simulating nonsorted circle development in arctic tundra ecosystems. *Journal of Geophysical Research: Biogeosciences*, *113*(G3), G03S06. https://doi.org/10.1029/2008JG000682

Daout, S., Doin, M. P., Peltzer, G., Socquet, A., & Lasserre, C. (2017). Large-scale InSAR monitoring of permafrost freeze-thaw cycles on the Tibetan Plateau. *Geophysical Research Letters*, *44*(2), 901–909. https://doi.org/10.1002/2016GL070781

Dehls, J. F., Larsen, Y., Marinkovic, P., Lauknes, T. R., Stødle, D., & Moldestad, D. A. (2019). INSAR.No: A national insar deformation mapping/monitoring service In Norway—From concept to operations. In *Proceedings of IGARSS 2019—IEEE International Geoscience and Remote Sensing Symposium* (pp. 5461–5464). https://doi.org/10.1109/IGARSS.2019.8898614

De Zan, F., Parizzi, P., Prats-Iraola, P., & López-Bekker, P. (2014). A SAR interferometric model for soil moisture. *IEEE Transactions on Geoscience and Remote Sensing*, *52*(1), 418–425. https://doi.org/10.1109/TGRS.2013.2241069

Dini, B., Daout, S., Manconi, A., & Loew, S. (2019). Classification of slope processes based on multitemporal DInSAR analyses in the Himalaya of NW Bhutan. *Remote Sensing of Environment*, *233*, 111408. https://doi.org/10.1016/j.rse.2019.111408

Dormann, C. F., Elith, J., Bacher, S., Buchmann, C., Gudrun, C., Carré, G., et al. (2013). Collinearity: A review of methods to deal with it and a simulation study evaluating their performance. *Ecography*, *36*, 27–46. https://doi.org/10.1111/j.1600-0587.2012.07348.x

Dormann, C. F., McPherson, J. M., Araújo, M. B., Bivand, R., Bolliger, J., Carl, G., et al. (2007). Methods to account for spatial autocorrelation in the analysis of species distributional data: A review. *Ecography*, *30*(5), 609–628. https://doi.org/10.1111/j.2007.0906-7590.05171.x

Eckerstorfer, M., Eriksen, H. Ø., Rouyet, L., Christiansen, H. H., Lauknes, T. R., & Blikra, L. H. (2018). Comparison of geomorphological field mapping and 2D-InSAR mapping of periglacial landscape activity at Nordnesfjellet, northern Norway. *Earth Surface Processes and Landforms*, *43*(10), 2147–2156. https://doi.org/10.1002/esp.4380

Eichel, J., Draebing, D., Klingbeil, L., Wieland, M., Eling, C., Schmidtlein, S., et al. (2017). Solifluction meets vegetation: The role of biogeomorphic feedbacks for turf-banked solifluction lobe development. *Earth Surface Processes and Landforms*, *42*(11), 1623–1635. https://doi.org/10.1002/esp.4102

Elith, J., Leathwick, J. R., & Hastie, T. (2008). A working guide to boosted regression trees. *Journal of Animal Ecology*, *77*(4), 802–813. https://doi.org/10.1111/j.1365-2656.2008.01390.x

Emardson, T. R., Simons, M., & Webb, F. H. (2003). Neutral atmospheric delay in interferometric synthetic aperture radar applications: Statistical description and mitigation. *Journal of Geophysical Research: Solid Earth*, *108*(B5), 2231. https://doi.org/10.1029/2002JB001781

Environmental Systems Research Institute (ESRI) (2019). *ArcGIS release 10.7.1*. Redlands, CA.

Eriksen, H. Ø., Bergh, S. G., Larsen, Y., Skrede, I., Kristensen, L., Lauknes, T. R., et al. (2017). Relating 3D surface displacement from satellite- and ground-based InSAR to structures and geomorphology of the Jettan rockslide, northern Norway. *Norwegian Journal of Geology*, *97*(4), 283–303. https://doi.org/10.17850/njg97-4-03

Eriksen, H. Ø., Lauknes, T. R., Larsen, Y., Corner, G. D., Bergh, S. G., Dehls, J., & Kierulf, H. P. (2017). Visualizing and interpreting surface displacement patterns on unstable slopes using multi-geometry satellite SAR interferometry (2D InSAR). *Remote Sensing of Environment*, *191*, 297–312. https://doi.org/10.1016/j.rse.2016.12.024

Etzelmüller, B., Hoelzle, M., Flo Heggem, E. S., Isaksen, K., Mittaz, C., Mühll, D. V., et al. (2001). Mapping and modeling the occurrence and distribution of mountain permafrost. *Norwegian Journal of Geography*, *55*(4), 186–194. https://doi.org/10.1080/00291950152746513

Farbrot, H., Isaksen, K., & Etzelmüller, B. (2008). Present and past distribution of mountain permafrost in Gaissane Mountains, Northern Norway. In Proceedings of the Ninth International Conference on Permafrost (Vol. 1, pp. 427–432). U.S.A.

Farbrot, H., Isaksen, K., Etzelmüller, B., & Gisnås, K. (2013). Ground thermal regime and permafrost distribution under a changing climate in northern Norway. *Permafrost and Periglacial Processes*, *24*(1), 20–38. https://doi.org/10.1002/ppp.1763

Ferretti, A., Prati, C., & Rocca, F. (2001). Permanent scatterers in SAR interferometry. *IEEE Transactions on Geoscience and Remote Sensing*, *39*(1), 8–20. https://doi.org/10.1109/36.898661

French, H. M. (2007). *The periglacial environment* (3rd ed.). Chichester, England: John Wiley & Sons.

Gisnås, K., Etzelmüller, B., Farbrot, H., Schuler, T. V., & Westermann, S. (2013). CryoGRID 1.0: Permafrost distribution in Norway estimated by a spatial numerical model. *Permafrost and Periglacial Processes*, *24*(1), 2–19. https://doi.org/10.1002/ppp.1765

Gisnås, K., Etzelmüller, B., Lussana, C., Hjort, J., Sannel, A. B. K., Isaksen, K., et al. (2017). Permafrost map for Norway, Sweden and Finland. *Permafrost and Periglacial Processes*, *28*(2), 359–378. https://doi.org/10.1002/ppp.1922

Goldstein, R. M., & Werner, C. L. (1998). Radar interferogram filtering for geophysical applications. *Geophysical Research Letters*, *25*(21), 4035–4038. https://doi.org/10.1029/1998GL900033

Grab, S. (2005). Aspects of the geomorphology, genesis and environmental significance of earth hummocks (thufur, pounus): Miniature cryogenic mounds. *Progress in Physical Geography*, *29*(2), 139–155. https://doi.org/10.1191/0309133305pp440ra

Gruber, S. (2020). Ground subsidence and heave over permafrost: Hourly time series reveal interannual, seasonal and shorter-term movement caused by freezing, thawing and water movement. *The Cryosphere*, *14*(4), 1437–1447. https://doi.org/10.5194/tc-14-1437-2020

Gruber, S., & Hoelzle, M. (2001). Statistical modeling of mountain permafrost distribution: Local calibration and incorporation of remotely sensed data. *Permafrost and Periglacial Processes*, *12*(1), 69–77. https://doi.org/10.1002/ppp.374

Guglielmin, M., Evans, C. J. E., & Cannone, N. (2008). Active layer thermal regime under different vegetation conditions in permafrost areas. A case study at Signy Island (Maritime Antarctica). *Geoderma*, *144*(1–2), 73–85. https://doi.org/10.1016/j.geoderma.2007.10.010

Haeberli, W., Noetzli, J., Arenson, L., Delaloye, R., Gärtner-Roer, I., Gruber, S., et al. (2010). Mountain permafrost: Development and challenges of a young research field. *Journal of Glaciology*, *56*(200), 1043–1058. https://doi.org/10.3189/002214311796406121

Harris, C., Arenson, L. U., Christiansen, H. H., Etzelmüller, B., Frauenfelder, R., Gruber, S., et al. (2009). Permafrost and climate in Europe: Monitoring and modeling thermal, geomorphological and geotechnical responses. *Earth-Science Reviews*, *92*(3–4), 117–171. https://doi.org/10.1016/j.earscirev.2008.12.002

Harris, C., & Davies, M. C. (2000). Gelifluction: Observations from large-scale laboratory simulations. *Arctic Antarctic and Alpine Research*, *32*(2), 202–207. https://doi.org/10.1080/15230430.2000.12003356

Harris, C., Davies, M. C., & Coutard, J. P. (1995). Laboratory simulation of periglacial solifluction: Significance of porewater pressures, moisture contents and undrained shear strengths during soil thawing. *Permafrost and Periglacial Processes*, *6*(4), 293–311. https://doi.org/10.1002/ppp.3430060403

Harris, C., Davies, M. C., & Coutard, J. P. (1997). Rates and processes of periglacial solifluction: An experimental approach. *Earth Surface Processes and Landforms*, *22*(9), 849–868. https://doi.org/10.1002/(sici)1096-9837(199709)22:9<849::aid-esp784>3.0.co;2-u

Harris, C., Kern-Luetschg, M., Murton, J., Font, M., Davies, M., & Smith, F. (2008). Solifluction processes on permafrost and non-permafrost slopes: Results of a large-scale laboratory simulation. *Permafrost and Periglacial Processes*, *19*(4), 359–378. https://doi.org/10.1002/ppp.630

Harris, C., Kern-Luetschg, M., Smith, F., & Isaksen, K. (2008). Solifluction processes in an area of seasonal ground freezing, Dovrefjell, Norway. *Permafrost and Periglacial Processes*, *19*, 31–47. https://doi.org/10.1002/ppp.609

Harris, C., Mühll, D. V., Isaksen, K., Haeberli, W., Sollid, J. L., King, L., et al. (2003). Warming permafrost in European mountains. *Global and Planetary Change*, *39*(3–4), 215–225. https://doi.org/10.1016/j.gloplacha.2003.04.001

Hinzman, L. D., Kane, D. L., Gieck, R. E., & Everett, K. R. (1991). Hydrologic and thermal properties of the active layer in the Alaskan Arctic. *Cold Regions Science and Technology*, *19*(2), 95–110. https://doi.org/10.1016/0165-232X(91)90001-W

Hjort, J. (2014). Which environmental factors determine recent cryoturbation and solifluction activity in a subarctic landscape? A comparison between active and inactive features. *Permafrost and Periglacial Processes*, *25*(2), 136–143. https://doi.org/10.1002/ppp.1808

Hjort, J., Karjalainen, O., Aalto, J., Westermann, S., Romanovsky, V. E., Nelson, F. E., et al. (2018). Degrading permafrost put Arctic infrastructure at risk by midcentury. *Nature Communications*, *9*, 5147. https://doi.org/10.1038/s41467-018-07557-4

Hjort, J., & Luoto, M. (2009). Interaction of geomorphic and ecologic features across altitudinal zones in a subarctic landscape. *Geomorphology*, *112*(3–4), 324–333. https://doi.org/10.1016/j.geomorph.2009.06.019

Hjort, J., & Luoto, M. (2011). Novel theoretical insights into geomorphic process–environment relationships using simulated response curves. *Earth Surface Processes and Landforms*, *36*(3), 363–371. https://doi.org/10.1002/esp.2048

Hjort, J., & Luoto, M. (2013). Statistical methods for geomorphic distribution modeling. In J. Schroder, & A. C. W. Baas (Eds.), Treatise on geomorphology. Quantitative modeling of geomorphology (Vol. 2, pp. 59–73). San Diego: Academic Press. https://doi.org/10.1016/B978-0-12-374739-6.00028-2

Hjort, J., Luoto, M., & Seppälä, M. (2007). Landscape scale determinants of periglacial features in subarctic Finland: A grid-based modeling approach. *Permafrost and Periglacial Processes*, *18*(2), 115–127. https://doi.org/10.1002/ppp.584

Hjort, J., Ujanen, J., Parviainen, M., Tolgensbakk, J., & Etzelmüller, B. (2014). Transferability of geomorphological distribution models: Evaluation using solifluction features in subarctic and Arctic regions. *Geomorphology*, *204*, 165–176. https://doi.org/10.1016/j.geomorph.2013.08.002

Isaksen, K., Farbrot, H., Blikra, L. H., Johansen, B., Sollid, J. L., & Eiken, T. (2008). Five year ground surface temperature measurements in Finnmark, Northern Norway. In Proceedings of the Ninth International Conference on Permafrost, Fairbanks, U.S.A. (Vol. 1, pp. 789–794).

Isaksen, K., Sollid, J. L., Holmlund, P., & Harris, C. (2007). Recent warming of mountain permafrost in Svalbard and Scandinavia. *Journal of Geophysical Research: Earth Surface*, *112*(F2), F02S04. https://doi.org/10.1029/2006JF000522

Jaesche, P., Veit, H., & Huwe, B. (2003). Snow cover and soil moisture controls on solifluction in an area of seasonal frost, eastern Alps. *Permafrost and Periglacial Processes*, *14*(4), 399–410. https://doi.org/10.1002/ppp.471

Jorgenson, M. T., Racine, C. H., Walters, J. C., & Osterkamp, T. E. (2001). Permafrost degradation and ecological changes associated with a warming climate in central Alaska. *Climatic Change*, *48*(4), 551–579. https://doi.org/10.1023/A:1005667424292

Kääb, A., Huggel, C., Fischer, L., Guex, S., Paul, F., Roer, I., et al. (2005). Remote sensing of glacier-and permafrost-related hazards in high mountains: An overview. *Natural Hazards and Earth System Sciences*, *5*(4), 527–554. https://doi.org/10.5194/nhess-5-527-2005

Karjalainen, O., Aalto, J., Luoto, M., Westermann, S., Romanovsky, V. E., Nelson, F. E., et al. (2019). Circumpolar permafrost maps and geohazard indices for near-future infrastructure risk assessments. *Scientific Data*, *6*, 190037. https://doi.org/10.1038/sdata.2019.37

Karjalainen, O., Luoto, M., Aalto, J., Etzelmuller, B., Grosse, G., Jones, B. M., et al. (2020). High potential for loss of permafrost landforms in a changing climate. *Environmental Research Letters*, *15*(10), 104065. https://doi.org/10.1088/1748-9326/abafd5

Kemppinen, J., Niittynen, P., Riihimäki, H., & Luoto, M. (2018). Modeling soil moisture in a high-latitude landscape using LiDAR and soil data. *Earth Surface Processes and Landforms*, *43*(5), 1019–1031. https://doi.org/10.1002/esp.4301

Knight, J., & Harrison, S. (2013). The impacts of climate change on terrestrial Earth surface systems. *Nature Climate Change*, *3*(1), 24–29. https://doi.org/10.1038/nclimate1660

Kojima, S. (1994). Relationships of vegetation, earth hummocks and topography in the high Arctic environment of Canada. In Proceedings of NIPR Symposium on Polar Biology (Vol. 7, pp. 256–269).

Konrad, J. M. (1999). Frost susceptibility related to soil index properties. *Canadian Geotechnical Journal*, *36*(3), 403–417. https://doi.org/10.1139/t99-008

Larsen, Y., Engen, G., Lauknes, T. R., Malnes, E., & Høgda, K. A. (2005). A generic differential interferometric SAR processing system, with applications to land subsidence and snow-water equivalent retrieval. In Proceedings of Fringe 2005 Workshop, Frascati, Italy, ESA SP-610 (Vol. 61).

Lauknes, T. R. (2011). InSAR tropospheric stratification delays: Correction using a small baseline approach. *IEEE Transactions on Geoscience and Remote Sensing*, *8*(6), 1070–1074. https://doi.org/10.1109/LGRS.2011.2156381

Lauknes, T. R., Zebker, H. A., & Larsen, Y. (2011). InSAR deformation time series using an L1-norm small-baseline approach. *IEEE Transactions on Geoscience and Remote Sensing*, *49*(1), 536–546. https://doi.org/10.1109/TGRS.2010.2051951

Legendre, P. (1993). Spatial autocorrelation: Trouble or new paradigm? *Ecology*, *74*(6), 1659–1673. https://doi.org/10.2307/1939924

Liu, L., Schaefer, K., Zhang, T., & Wahr, J. (2012). Estimating 1992–2000 average active layer thickness on the Alaskan North Slope from remotely sensed surface subsidence. *Journal of Geophysical Research: Earth Surface*, *117*(F1), F01005. https://doi.org/10.1029/2011JF002041

Luoto, M., & Hjort, J. (2006). Scale matters—A multi-resolution study of the determinants of patterned ground activity in subarctic Finland. *Geomorphology*, *80*(3–4), 282–294. https://doi.org/10.1016/j.geomorph.2006.03.001

Martin, L. C. P., Nitzbon, J., Aas, K. S., Etzelmüller, B., Kristiansen, H., & Westermann, S. (2019). Stability conditions of peat plateaus and palsas in northern Norway. *Journal of Geophysical Research: Earth Surface*, *124*(3), 705–719. https://doi.org/10.1029/2018JF004945

Massonnet, D., & Feigl, K. L. (1998). Radar interferometry and its application to changes in the Earth's surface. *Reviews of Geophysics*, *36*(4), 441–500. https://doi.org/10.1029/97RG03139

Matsuoka, N. (2001). Solifluction rates, processes and landforms: A global review. *Earth-Science Reviews*, *55*(1–2), 107–134. https://doi.org/10.1016/S0012-8252(01)00057-5

Matsuoka, N., Abe, M., & Ijiri, M. (2003). Differential frost heave and sorted patterned ground: Field measurements and a laboratory experiment. *Geomorphology*, *52*(1–2), 73–85. https://doi.org/10.1016/S0169-555X(02)00249-0

Matsuoka, N., Hirakawa, K., Watanabe, T., & Moriwaki, K. (1997). Monitoring of periglacial slope processes in the Swiss Alps: The first two years of frost shattering, heave and creep. *Permafrost and Periglacial Processes*, *8*, 155–177. https://doi.org/10.1002/(sici)1099-1530(199732)8:2<155::aid-ppp248>3.0.co;2-n

Morgenstern, N. R., & Nixon, J. F. (1971). One-dimensional consolidation of thawing soils. *Canadian Geotechnical Journal*, *8*, 558–565. https://doi.org/10.1139/t71-057

NCCS (2021). *Observations and weather statics*. Norwegian Centre for Climate Services (NCCS). Retrieved from https://seklima.met.no/observations/

Nelson, F. E., Anisimov, O. A., & Shiklomanov, N. I. (2002). Climate change and hazard zonation in the circum-Arctic permafrost regions. *Natural Hazards*, *26*(3), 203–225. https://doi.org/10.1023/A:1015612918401

NGU (2020). *InSAR Norway*. Retrieved from www.insar.no

Nicolsky, D. J., Romanovsky, V. E., Tipenko, G. S., & Walker, D. A. (2008). Modeling biogeophysical interactions in nonsorted circles in the Low Arctic. *Journal of Geophysical Research: Biogeosciences*, *113*(G3), G03S05. https://doi.org/10.1029/2007JG000565

Niittynen, P., Heikkinen, R. K., & Luoto, M. (2018). Snow cover is a neglected driver of Arctic biodiversity loss. *Nature Climate Change*, *8*(11), 997–1001. https://doi.org/10.1038/s41558-018-0311-x

Niittynen, P., Heikkinen, R. K., & Luoto, M. (2020). Decreasing snow cover alters functional composition and diversity of Arctic tundra. *Proceedings of the National Academy of Sciences*, *117*(35), 21480–21487. https://doi.org/10.1073/pnas.2001254117

Niittynen, P., & Luoto, M. (2018). The importance of snow in species distribution models of arctic vegetation. *Ecography*, *41*(6), 1024–1037. https://doi.org/10.1111/ecog.03348

NMA (2016). *DTM 10 Terrengmodell (UTM33)*. Norwegian mapping authority. Retrieved from https://kartkatalog.geonorge.no/

NMA (2020a). *Toporaster 4 WMS*. Norwegian mapping authority. Retrieved from https://kartkatalog.geonorge.no/

NMA (2020b). *Norge i bilder WMTS (Euref89 UTM33). Images 115 (Finnmark 2011-08-15), 217 (2016-08-18) and 118 (Finnmark 2018-07-19)*. Norwegian mapping authority. Retrieved from https://www.norgeibilder.no/

Obu, J., Westermann, S., Barboux, C., Bartsch, A., Delaloye, R., Grosse, G., & Wiesmann, A. (2020). *ESA permafrost climate change initiative (Permafrost_cci): Permafrost active layer thickness for the northern hemisphere, v2.0*. Centre for Environmental Data Analysis. https://doi.org/10.5285/29c4af5986ba4b9c8a3cfc33ca8d7c85

Obu, J., Westermann, S., Bartsch, A., Berdnikov, N., Christiansen, H. H., Dashtseren, A., et al. (2019). Northern Hemisphere permafrost map based on TTOP modeling for 2000–2016 at 1 km^2 scale. *Earth-Science Reviews*, *193*, 299–316. https://doi.org/10.1016/j.earscirev.2019.04.023

Olson, D. M., Dinerstein, E., Wikramanayake, E. D., Burgess, N. D., Powell, G. V., Underwood, E. C., et al. (2001). Terrestrial ecoregions of the world: A new map of life on Earth: A new global map of terrestrial ecoregions provides an innovative tool for conserving biodiversity. *BioScience*, *51*(11), 933–938. https://doi.org/10.1641/0006-3568(2001)051[0933:teotwa]2.0.co;2

Peterson, R. A., & Krantz, W. B. (2008). Differential frost heave model for patterned ground formation: Corroboration with observations along a North American arctic transect. *Journal of Geophysical Research: Biogeosciences*, *113*(G3), G03S04. https://doi.org/10.1029/2007JG000559

Peterson, R. A., Walker, D. A., Romanovsky, V. E., Knudson, J. A., Raynolds, M. K., & Krantz, W. B. (2003). A differential frost heave model: Cryoturbation-vegetation interactions. *Proceedings of the Eighth International Conference on Permafrost, Lisse, Zürich, Switzerland. AA Balkema* (Vol. *2*, pp. 885–890).

Porter, C., Morin, P., Howat, I., Noh, M. J., Bates, B., Peterman, K., et al. (2018). ArcticDEM (Vol. 1). Harvard Dataverse.

Reinosch, E., Buckel, J., Dong, J., Gerke, M., Baade, J., & Riedel, B. (2020). InSAR time series analysis of seasonal surface displacement dynamics on the Tibetan Plateau. *The Cryosphere*, *14*(5), 1633–1650. https://doi.org/10.5194/tc-14-1633-2020

Rempel, A. W. (2007). Formation of ice lenses and frost heave. *Journal of Geophysical Research: Earth Surface*, *112*(F2), F02S21. https://doi.org/10.1029/2006JF000525

Ridefelt, H., Åkerman, J., Beylich, A. A., Boelhouwers, J., Kolstrup, E., & Nyberg, R. (2009). 56 years of solifluction measurements in the abisko mountains, northern sweden–analysis of temporal and spatial variations of slow soil surface movement. *Geografiska Annaler - Series A: Physical Geography*, *91*(3), 215–232. https://doi.org/10.1111/j.1468-0459.2009.00365.x

Ridefelt, H., Etzelmüller, B., & Boelhouwers, J. (2010). Spatial analysis of solifluction landforms and process rates in the Abisko Mountains, northern Sweden. *Permafrost and Periglacial Processes*, *21*(3), 241–255. https://doi.org/10.1002/ppp.681

Romanovsky, V. E., Smith, S. L., & Christiansen, H. H. (2010). Permafrost thermal state in the polar Northern Hemisphere during the international polar year 2007–2009: A synthesis. *Permafrost and Periglacial Processes*, *21*(2), 106–116. https://doi.org/10.1002/ppp.689

Rouse, J. W., Haas, R. H., Schell, J. A., & Deering, D. W. (1974). Monitoring vegetation systems in the Great Plains with ERTS. In *Proceedings of the Third Earth Resources Technology Satellite-1 Symposium, NASA, Washington, D.C.* (pp. 309–317).

Rouyet, L., Lauknes, T. R., Christiansen, H. H., Strand, S. M., & Larsen, Y. (2019). Seasonal dynamics of a permafrost landscape, Adventdalen, Svalbard, investigated by InSAR. *Remote Sensing of Environment*, *231*, 111236. https://doi.org/10.1016/j.rse.2019.111236

Rudy, A. C., Lamoureux, S. F., Treitz, P., Short, N., & Brisco, B. (2018). Seasonal and multi-year surface displacements measured by DInSAR in a High Arctic permafrost environment. *International Journal of Applied Earth Observation and Geoinformation*, *64*, 51–61. https://doi.org/10.1016/j.jag.2017.09.002

Rudy, A. C. A., Lamoureux, S. F., Treitz, P., Ewijk, K. V., Bonnaventure, P. P., & Budkewitsch, P. (2017). Terrain controls and landscape-scale susceptibility modeling of active-layer detachments, Sabine Peninsula, Melville Island, Nunavut. *Permafrost and Periglacial Processes*, *28*, 79–91. https://doi.org/10.1002/ppp.1900

Schuh, C., Frampton, A., & Christiansen, H. H. (2017). Soil moisture redistribution and its effect on inter-annual active layer temperature and thickness variations in a dry loess terrace in Adventdalen, Svalbard. *The Cryosphere*, *11*(1), 635–651. https://doi.org/10.5194/tc-11-635-2017

Seppälä, M. (2011). Chapter 3. Periglacial phenomena of northern Fennoscandia. In J. Boardman (Ed.), *Periglacial processes and landforms in Britain and Ireland* (pp. 45–55). Cambridge University Press.

Shiklomanov, N. I., Streletskiy, D. A., & Nelson, F. E. (2012). Northern hemisphere component of the global circumpolar active layer monitoring (CALM) program. In Proceedings of the 10th International Conference on Permafrost, Salekhard, Russia (Vol. 1, pp. 377–382).

Shiklomanov, N. I., Streletskiy, D. A., Nelson, F. E., Hollister, R. D., Romanovsky, V. E., Tweedie, C. E., et al. (2010). Decadal variations of active-layer thickness in moisture-controlled landscapes, Barrow, Alaska. *Journal of Geophysical Research: Biogeosciences*, *115*(G4), G00I04. https://doi.org/10.1029/2009JG001248

Smith, D. J. (1987). Frost-heave activity in the Mount Rae area, Canadian Rocky Mountains. *Arctic and Alpine. Research*, *19*(2), 155–166. https://doi.org/10.2307/1551248

Strozzi, T., Antonova, S., Günther, F., Mätzler, E., Vieira, G., Wegmüller, U., et al. (2018). Sentinel-1 SAR interferometry for surface deformation monitoring in low-land permafrost areas. *Remote Sensing*, *10*(9), 1360. https://doi.org/10.3390/rs10091360

Thomas, H. R., Cleall, P., Li, Y. C., Harris, C., & Kern-Luetschg, M. (2009). Modeling of cryogenic processes in permafrost and seasonally frozen soils. *Géotechnique*, *59*(3), 173–184. https://doi.org/10.1680/geot.2009.59.3.173

Thuiller, W., Lafourcade, B., Engler, R., & Araujo, M. B. (2009). BIOMOD—A platform for ensemble forecasting of species distributions. *Ecography*, *32*, 369–373. https://doi.org/10.1111/j.1600-0587.2008.05742.x

Van Vliet-Lanoë, B. (1991). Differential frost heave, load casting and convection: Converging mechanisms; a discussion of the origin of cryoturbations. *Permafrost and Periglacial Processes*, *2*(2), 123–139. https://doi.org/10.1002/ppp.3430020207

Virtanen, R., Oksanen, L., Oksanen, T., Cohen, J., Forbes, B. C., Johansen, B., et al. (2016). Where do the treeless tundra areas of northern highlands fit in the global biome system: Toward an ecologically natural subdivision of the tundra biome. *Ecology and Evolution*, *6*(1), 143–158. https://doi.org/10.1002/ece3.1837

Walsh, S. J., Butler, D. R., & Malanson, G. P. (1998). An overview of scale, pattern, process relationships in geomorphology: A remote sensing and GIS perspective. *Geomorphology*, *21*(3–4), 183–205. https://doi.org/10.1016/S0169-555X(97)00057-3

Wang, C., Zhang, Z., Zhang, H., Zhang, B., Tang, Y., & Wu, Q. (2018). Active layer thickness retrieval of Qinghai–Tibet permafrost using the TerraSAR-X InSAR technique. *IEEE Journal of Selected Topics in Applied Earth Observations and Remote Sensing*, *11*(11), 4403–4413. https://doi.org/10.1109/JSTARS.2018.2873219

Westermann, S., Duguay, C. R., Grosse, G., & Kääb, A. (2015). Chapter 13. Remote sensing of permafrost and frozen ground. In M. Tedesco (Ed.), *Remote sensing of the cryosphere* (1st ed.). John Wiley & Sons.

Wilson, P., & Sellier, D. (1995). Active patterned ground and cryoturbation on Muckish mountain, Co. Donegal, Ireland. *Permafrost and Periglacial Processes*, *6*(1), 15–25. https://doi.org/10.1002/ppp.3430060104

Zebker, H. A., Rosen, P. A., & Hensley, S. (1997). Atmospheric effects in interferometric synthetic aperture radar surface deformation and topographic maps. *Journal of Geophysical Research: Solid Earth*, *102*(B4), 7547–7563. https://doi.org/10.1029/96JB03804

Zwieback, S., & Hajnsek, I. (2014). The impact of vegetation growth on DInSAR coherence regions and estimated deformations. In *Proceedings of IEEE geoscience and remote sensing Symposium* (pp. 966–969). https://doi.org/10.1109/igarss.2014.6946587

Zwieback, S., Hensley, S., & Hajnsek, I. (2015). Assessment of soil moisture effects on L-band radar interferometry. *Remote Sensing of Environment*, *164*, 77–89. https://doi.org/10.1016/j.rse.2015.04.012

Zwieback, S., Liu, X., Antonova, S., Heim, B., Bartsch, A., Boike, J., & Hajnsek, I. (2016). A statistical test of phase closure to detect influences on DInSAR deformation estimates besides displacements and decorrelation noise: Two case studies in high-latitude regions. *IEEE Transactions on Geoscience and Remote Sensing*, *54*(9), 5588–5601. https://doi.org/10.1109/tgrs.2016.2569435